A RESEARCH REPORT ON

Unveiling the structure of Giant Radio Galaxies J0133-1302 and J2256-3617

A RESEARCH REPORT SUBMITTED TO THE FACULTY OF SCIENCE,
UNIVERSITY OF WITWATERSRAND, JOHANNESBURG
IN PARTIAL FULFILLMENT OF THE REQUIREMENTS
FOR THE DEGREE OF MASTER OF SCIENCE.

MASTER OF SCIENCE

(Astrophysics)

BY

Tebogo Bestina Mashile **Student No:802808**

Under the Guidance of

Dr Mhlahlo N

Faculty of Science

Department of Physics,

2021

DECLARATION

I declare that this research report is my own, unaided work. It is being submitted for the Degree of Master of Science at the University of the Witwatersrand, Johannesburg. It has not been submitted before for any degree or examination at any other University.

________________________ 23/08/21

(Signature of candidate) Date

23 day of August 20 21 at Pretoria

ABSTRACT

The follow-up data from the Giant Metrewave Radio Telescope (GMRT) at two different frequencies, i.e. 325 MHz and 610 MHz were reduced and imaged separately, and the radio sources in an area of the sky in RA:$01^h33^m10^s$ and DEC: -13°$01'$59", and RA:$22^h56^m15^s$ and DEC: -36°$17'$59" were detected. The research study focus on previously KAT-7 discovered giant radio galaxy (GRG) J0133-1303, and GRG J2256-3617 which was never studied before, presenting a detailed analysis of their morphology, a spectral index map between 325 MHz and 610 MHz for both GRGs and a spectral index map between 325 MHz and 1400 MHz for the GRG J2256-3617 and multi-frequency associated with their optical counterparts. These two GRGs have the FR II radio morphology, but no radio jets are detected. The GRG J0133-1303 has an overall projected size of ∼3.59 Mpc. The radio core has flat spectral index, and inverted spectrum, which indicate the restarting nuclear activity. At the photometric redshift $z \approx 0.3$, the GRG J0133-1303 has a radio power of $P_{1.4GHz} \approx 0.16$ x 10^{24} W Hz^{-1}, which is compatible with the typical radio powers of the GRGs. The GRG J2256-3617 appears to have an inverted spectrum but this is not conclusive, hence, more data at low frequency are required to conclude this. This radio source has overall projected size of ∼ 1.57 Mpc. The GRG J2256-3617 has a radio power of $P_{1.4GHz} \approx 0.19$ x 10^{24} W Hz^{-1} at the photometric redshift of $z \approx 0.09$.

DEDICATION

Firstly, I dedicate this research report to my parents (Rinos and Leah Mashile) for being there for me throughout the entire masters research work. I would not be the person I am today if it was not for them.

Secondly, I dedicate this to my siblings (Kagisho, Thabang, Katlego, Tshegofatso and Samson Mashile) who supported me throughout my studies. A special feeling of gratitude to my son, Mogau Lesedi, for being my pillar of strength.

ACKNOWLEDGEMENTS

Firstly, I would like to thank God for everything he has done for me and making everything possible. Thanks to my supervisor, Dr Nceba Mhlahlo for coming up with this project scope and taking me every step for this research.

I would like to extended my gratitude to my line manager at the Department of Science and Innovation for his support and giving me time to work on my research project.

I would like to acknowledge my friends in the Astrophysics group at Wits for their support and discussions, particularly Siphiwe, Nthabiseng and Rowan.

I would also like to extend my appreciation to Professor Carignan Claude for making time out of his busy schedule to give advice and guidance.

Lastly, but not least, I acknowledge funding support from the Square Kilometre Array South Africa initiative through Young Professionals Development Programme.

TABLE OF CONTENTS

LIST OF FIGURES

LIST OF TABLES

LIST OF SYMBOLS

α	Spectral index
ν	frequency
S	Integrated flux density
z	Redshift
σ	Uncertainties of the flux density

NOMENCLATURE

AGN	Active Galactic Nuclei
AIPS	Astronomical Imaging Process System
ALMA	Atacama Large Millimeter Array
APM	Automated Plate Measurement
BP	Bandpass
CASA	Common Astronomy Software Applications
DDRG	Double-Double Radio Galaxy
DDRQ	Double-Double Radio Quasar
DEC	Declination
DSS	Digitized Sky Survey
ESO	European Southern Observatoryry
FR I	Fanaroff and Riley type 1
FR II	Fanaroff and Riley type 2
GHz	GigaHertz
GLEAM	Galactic and Extragalactic All-sky Murchison
GMRT	Giant Metrewave Radio Telescope
GRG	Giant Radio Galaxy
IGM	Intergalactic Medium
IR	Infrared
Jy	Jansky
KAT-7	Karoo Array Telescope
kpc	kiloparesc

MHz	MegaHertz
Mpc	Megaparsec
MWA	Murchison Widefield Array
NRAO	National Radio Astronomy Observatory
NAT	Narrow Angle Tailed
NVSS	NRAO VLA Sky Survey
OVV	Optically Violet Variable
QSO	Quasi-Stellar Objects
RA	Right ascension
RFI	Radio Frequency Interference
RG	Radio Galaxy
SPAM	Source Peeling and Atmospheric Modelling
SKA	Square Kilometre Array
SMBH	Supermasive Black Hole
SUMSS	Sydney University Molonglo Sky Survey
TIFR	Tata Institute of Fundamental Research
TGSS	TIFR GMRT Sky Survey
VLA	Very Large Array
VLAAS	VLA All Sky Survey

CHAPTER 1

INTRODUCTION

1.1 BACKGROUND

The active galactic nuclei (AGNs) are astrophysical objects which display an active core surrounded by an accretion disc, and are the brightest objects in the universe. These sources are classified into different groups, namely: Quasars, Seyfert-galaxies, Radio Galaxies (RGs), and BL Lacertae (BL Lacs) objects and Blazars. Some of the RGs are distinguished by massive structures and are known as Giant Radio Galaxies (GRGs). The GRGs have an overall projected linear size of >0.7 Megapersec (Mpc), and are considered to be the biggest astrophysical objects within the universe (Dabhade *et al.*, 2017). They represent massive and most active single bodies and it is very likely that they form a significant part in the evolution of large-scale structures.

GRGs are of great importance in the acceleration of cosmic rays covering massive cosmic scales, in the feedback mechanism of AGNs into the intergalactic and intracluster medium and in the seeding of large-scale magnetic fields within the universe. These massive radio sources can also be used in determining the entire jet or radio lobe energetics in AGN-dominated structure (Colafrancesco *et al.*, 2016). GRGs are not fully understood, are very few ~ 300 and not easily detectable over larger parts of the sky. It is still not clear what could be the conditions that result in the formation of GRGs. It may be the unusual internal properties of the source central engine or external conditions (Komberg and Pashchenko, 2009).

Two fundamental scenarios have been developed to describe the exceptional sizes of the GRGs. First, the lobes could be fed by very powerful central engines which will supply the jets with the essential thrust to bore their long way through the ambient medium and secondly, GRGs could be normal radio sources evolving in very low-density environments contributing small resistance to the evolution of the jets (Lara *et al.*, 2000). Discovering more of these radio sources is critical in order to study their properties in more details and how they interact with their environment.

This research project will focus on two giant radio galaxies GRG J0133-1303, previously observed using seven dish Karoo Array Telescope (KAT-7) in the KAT-7 field of ACO209, and GRG J2256-3617 observed with the GMRT. The important questions that the research study aim to answer are, to determine the type of radio morphology and properties associated with these radio sources, and their projected size. The GRGs are believed to be RGs grown into massive structure, and their huge size is because they evolve in regions of low density environment or fuelled by the source central engine, which empowers them to grow comparatively fast (Dabhade *et al.*, 2020*b*). Understanding how the radio jets interact with their host galaxies and broader environment is significant to understanding how galaxies form and evolve with time. To date, this remains as one of astronomy's key unanswered questions.

1.2 PURPOSE OF THE STUDY

1.2.1 Aim

The purpose of this research project is to study the GRG J0133-1303 discovered in the KAT-7 field of ACO209, and GRG J2256-3617, to gain a better understanding on detailed analysis of their morphology and properties. The KAT-7 telescope previously uncovered the extended emission into two components while the NVSS resolved the radio source (GRG J0133-1303) into four components, and there is no detailed work on GRG J2256-3617. Hence, in order to study the properties and nature of these two radio sources in detail at low frequency, GMRT follow-up data were used. The research study also used data available on other radio surveys and the capability to resolve the two radio sources for studies of their properties and nature.

1.2.2 Objectives

The objectives of the research project will be to:

- Search for the radio core, jets, lobes and characterize the radio source.
- Determine the type of radio morphology associated with the radio source.
- Measure the projected size of the GRG.
- Perform the spectral analysis of the radio source.

1.2.3 Questions

The research project seek to address the following questions:

- What type of radio morphology is associated with the radio source?
- What is the projected size of the GRG?

1.3 RESEARCH REPORT OUTLINE

To answer the three aforementioned questions, the research study is divided into six chapters which are logically forming a continuous unit. Chapter 1 provides a general introduction on the background to the study, and also defines the aim of the research, objectives, and questions. The literature review is reported in Chapter 2 structured as follows: in Section 2.1 AGN properties are discussed, particularly their classes; Section 2.2 the properties of RGs are discussed in full details, this includes their structure, and spectral ageing; Section 2.3 gives the description of the unification model; Section 2.4 the GRGs are introduced with brief details of their properties, and formation and evolution; and finally Section 2.5 and Section 2.6 give the background of GRG J0133-1303 and J2256-3617, respectively.

Chapter 3 is a detailed data acquisition and reduction followed throughout the research project, this includes the software packages used for data analysis and imaging techniques. It is structured as follows, Section 3.1 gives a full details of the full data, data reduction, and

Imaging. Section 3.2 is the Archival Data obtained from different surveys. The results of the research project are reported in Chapter 4 and 5. Finally, Chapter 6 is a general conclusion of the results of the research project. The figures and tables are consolidated within the chapters, followed by references at the end of this report.

CHAPTER 2

LITERATURE REVIEW

2.1 AGNs

Active Galactic Nuclei (AGNs) are considered to be the galaxies that have very bright and active nuclei. Beside being the foremost powerful and luminous astrophysical objects within the universe, AGNs are distinguished by being strong emitters at any range of the electromagnetic spectrum (Perucho *et al.*, 2015). These galaxies are made from supermassive black holes (SMBHs) surrounding accretion system (Krawczynski and Treister, 2013). An AGN can play a critical part within the intergalactic, interstellar and intracluster medium due to their interaction with their environment (Mahatma, 2017). An insight on the dynamics of an AGN is significant in understanding how the universe is formed and evolves. Figure 2.1 is an illustration of how a typical powerful AGN looks like. In modern studies, RGs, Quasars, Seyfert-galaxies, and BL Lacs objects and Blazars have been classified into different groups of AGN.

2.1.1 Quasars

Galaxies exhibiting broad emission lines became well known after the discovery of the Seyfert galaxies. This lead to the discovery of the first brightest classes of AGN known as quasars in the 1950s (Shields, 1999). Due to poor sensitivity of the telescopes back then, some compact sources were unidentified, while some radio sources were identified as Galactic supernova remnants or radio galaxies (see 2.2 for more details). The radio source 3C48 which was studied using optical telescopes, presented a broad emission lines within the optical spectrum, which was unusual during that period for an object to emit high luminosity at radio wavelengths (Matthews and Sandage, 1963). There was evidence for an extragalactic origin as the source was found to have a redshift of $z \approx 0.37$ (Mahatma, 2017). More radio sources of this nature were later discovered using Lovell telescope and other telescopes. These

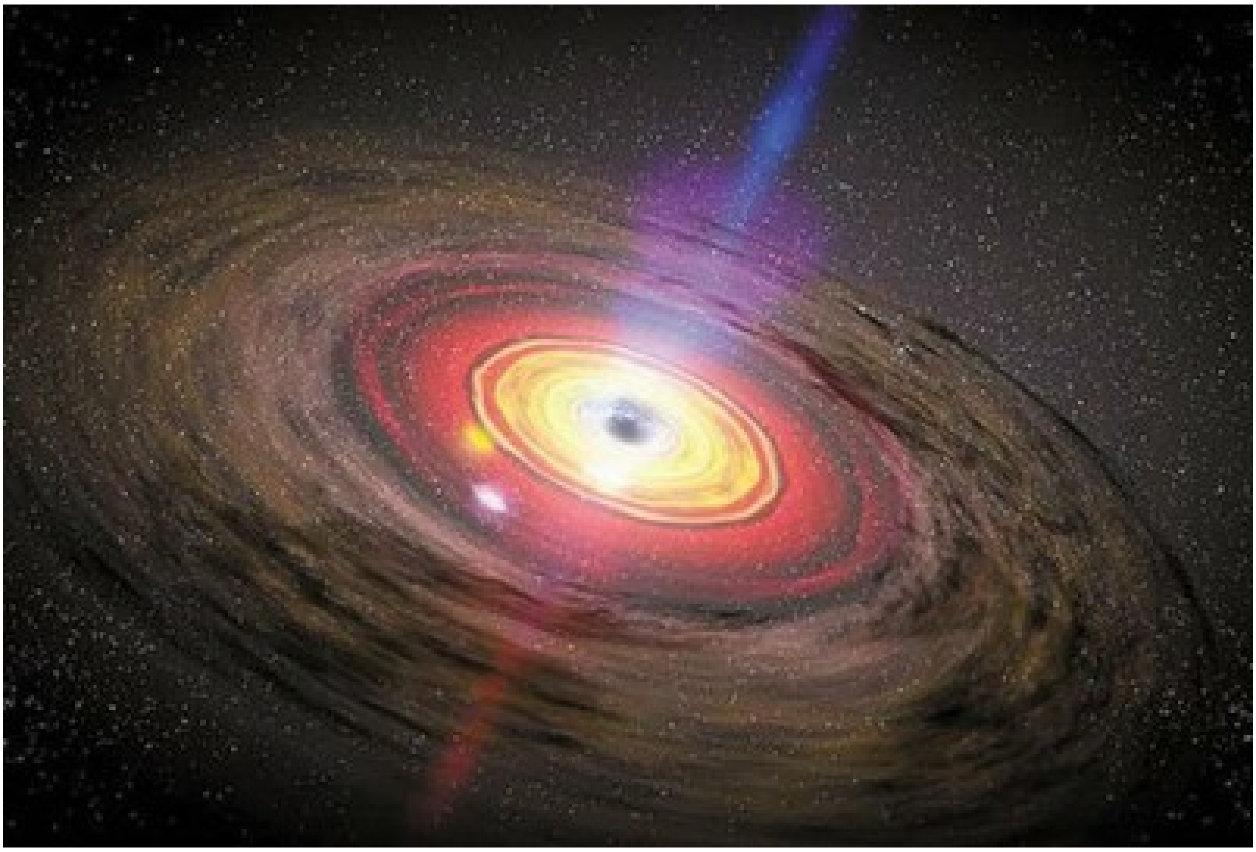

Figure 2.1: An artist impression of of an AGN with the accretion disc around the SMBH. Credit: *NASA / Dana Berry, SkyWorks Digital*

ultra luminous sources classified as quasars were later found to have a brightest nucleus of an energetic galaxy with an accreting SMBH.

2.1.2 Seyfert Galaxies

Seyfert galaxies, named after Carl Keenan Seyfert, and quasars are the two biggest classes of active sources. The Seyfert galaxies were first discovered in 1908. This was followed by the discovery of more Seyfert galaxies which looked similar to a well known Seyfert galaxy NGC 1068 in Cetus, with description of broad emission lines in 1943 (Seyfert, 1943). The broad lines became a characteristic feature observed in what is presently called 'active galaxies' as they were usually not observed in normal galaxies. The Seyfert galaxies are spiral in morphology with luminous quasar-like nuclei, very high surface brightnesses with an optical spectra that reveals strong, high-ionisation emission lines (Peterson, 1997).

The Seyfert galaxies which account approximately for 10% of all galaxies are divided into two sub-classes according to the respective size of emission lines appearing on their spectra. They are most well studied astronomical objects, as they are thought to be fuelled by the same marvels that happen in quasars, in spite of the fact that they are closer and marginally less bright than quasars. The Type 1 Seyfert galaxies have a narrow, and broad line peaks in their spectrum. The continuum emission from these Seyfert galaxies appears to be weak at long wavelength (radio), but strong at most wavelengths. Type II Seyfert galaxies are characterised by the luminous active nucleus, and they also appears bright when observed at infra-red wavelengths. Their spectra has broad lines correlated to strong dipole or inter-combination transitions, while the narrow lines is correlated with forbidden transitions (Pradhan and Nahar, 2011).

2.1.3 BL Lacertae objects and Blazars

The BL Lacertae sources (BL Lacs) were another group of AGN to be detected. These objects were at first thought to be stars because of exhibiting unusual spectra with neither emission nor absorption lines, and very bright at radio wavelengths. These objects are considered to have a flat spectrum which takes a form $S_\nu \sim \nu^{-\alpha}$, with S as the integrated flux density, α is the spectral index, and ν the frequency. The BL Lacs were found to have some similar characteristics with radio-loud quasars. Both radio-loud quasars and the BL Lacs possess a power-law formation on the Infra-Red optical spectra and are luminous in the radio wavelengths as compared to optical. In the middle of the 1970's, there was an evidence of another AGN with similar characteristic to these class of objects, showing strong variability and powerful linear polarisation. The variability of these AGN was ascertained to be inconsistent, mostly with long period of stability and this was followed by a speedy blazing in days. What made this class of AGNs called 'Optically Violent Variable' (OVV) quasars to be unique from BL Lacs was the robust optical emission and broad lines features, which are different from the continuum emission observed in the classical BL Lacs.

The BL Lacs and OVV quasars are seen as separate sources for observational purpose but are collectively known as Blazars. Using Very Long Baseline Interferometry (VLBI) techniques, a jet structure near an active nucleus of the OVV qausars was identified with 'blobs' of emission at long wavelengths (Mahatma, 2017). The BL Lacs, Blazars and Radio-loud quasars grouped together are called 'radio-loud AGN'. Additional class of radio-loud AGN called RGs with an extended structure to Mpc scales was later discovered.

2.2 RADIO GALAXIES

RGs which are the brightest and exhibit a broader scope of structures at radio wavelengths were first discovered in the 1950s (Jennison and Gupta, 1953). Since then many of them have been discovered. RGs are amongst the biggest single bodies within the cosmos alongside the group of radio relics and halos (Dabhade *et al.*, 2020*a*).

2.2.1 Structure of Radio Galaxies

RGs are normally characterised by the core, radio lobes, and jets with an AGN as host galaxy (Dabhade *et al.*, 2020*b*). The most usual large-scale structures are double radio lobes. These double radio lobes are fairly symmetrical structures attached to the active nucleus on both sides. Some of the RGs have one or two long narrow features known as jets, connecting the lobes with the core. The term jet is usually used to mention both the observable feature and the underlying flow. A tiny compact region with high emission where the jets reaches the outer edge of the radio lobes is called a hotspot. They are seen as the shock front with the intergalactic medium. These features are illustrated in Figure 2.2.

The radio sources are categorised into two different classes called Fanaroff and Riley I, and II (see Figure 2.3). This distinction was originally categorised according to the brightness distribution within the radio lobes (De Young, 1976). Most GRGs display FR II radio morphology with relatively low radio power. The Fanaroff Riley classification is used to differentiate RGs with active nuclei according to their radio luminosity of their radio emissions in relation to their hosting environment (Fanaroff and Riley, 1974). The luminosity of the radio sources with the FR I radio morphology becomes less bright as the distance from the core increase, while the sources with the FR II radio morphology are very bright within the radio lobes, which means they are efficient in transporting energy.

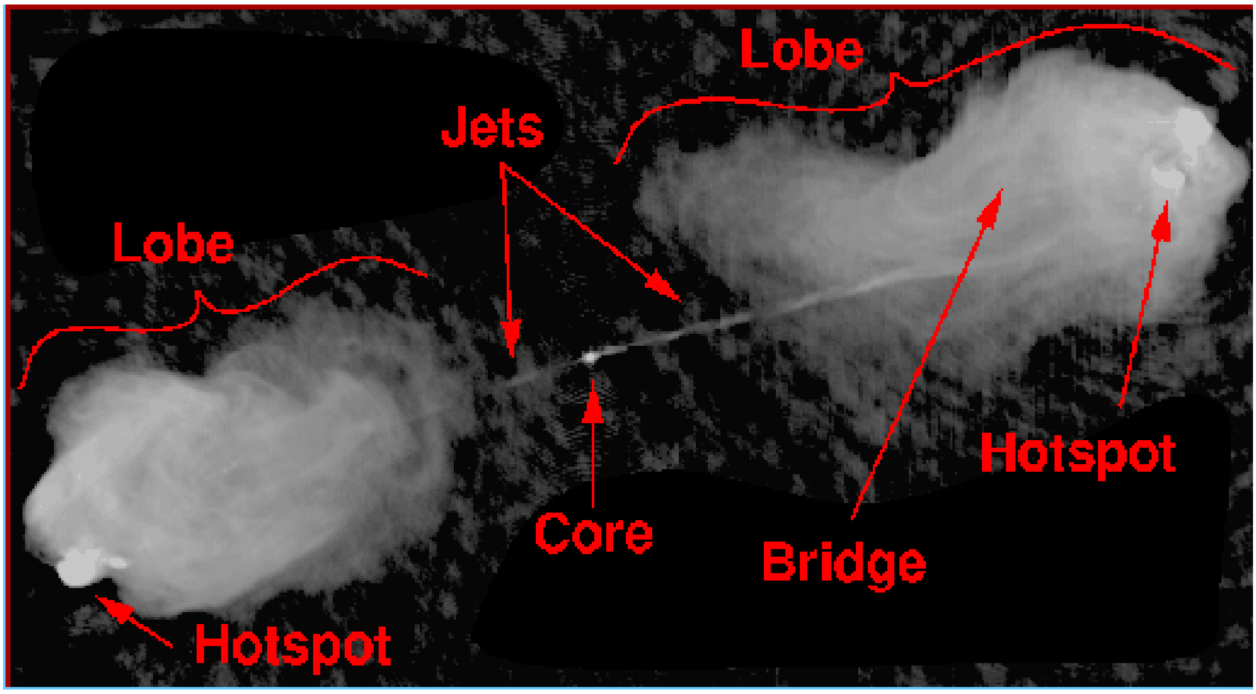

Figure 2.2: A radio galaxy image with the main features described (De Young, 1976).

The double-double radio galaxies (DDRGs) which undergo more than one cycle of jet activity are rare examples of AGNs (Hunik and Jamrozy, 2016). Although most DDRGs are associated with radio galaxies, there are some quasar that exhibit episodic activity, and only few of them have been reported to date. To understand what causes the process of mechanism for jet activity in these sources, and the properties of the parent galaxies and their environments, more of these sources need to be identified. The most promising double-double radio quasar reported is J0935+0204 (4C 02.27), at the redshift z = 0.65 (Jamrozy *et al.*, 2009). J0935+0204 (4C 02.27) is reported to have a blue-continuum-dominated spectrum, with projected linear sizes of ∼470 kpc for the outer radio lobe and ∼70 kpc for the inner radio lobe (Nandi *et al.*, 2014).

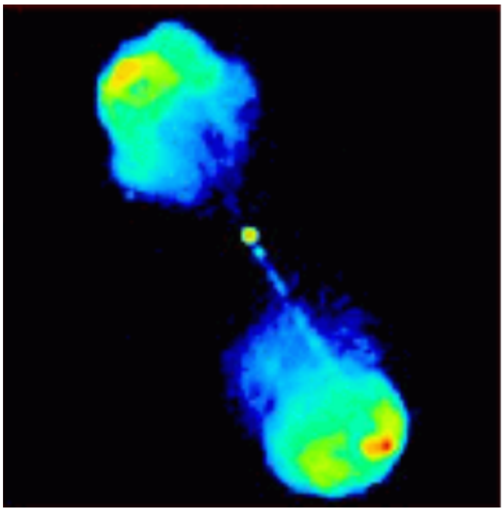

(a) FR II

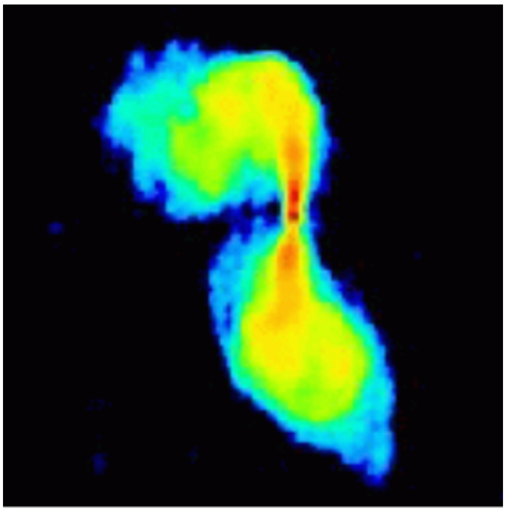

(b) FR I

Figure 2.3: An FR II radio source, 3C272 (Leahy, 1996) (a) and an FR I radio source, C47(b)(Laing and Bridle, 1987).

The DDRG, shown in Figure 2.4 is characterised by a doubled radio lobe with the same central AGN (Schoenmakers *et al.*, 2000). The double lobe of the radio source appears to be unequally sized, two-sided, edge brightened. In many instances, the dispersed outer lobes are in-line with the inner lobes in the range of kpc to Mpc, while the luminous inner lobes stretches from parsec to few 100 kpc (Nandi *et al.*, 2019). The active nucleus of the two RGs merge, with the smaller structure positioned inside the bigger structure, appearing as two independent structures with FR II type radio morphology (Kaiser *et al.*, 2000). This radio morphology is what makes the DDRGs to be different from the normal FR II sources. In addition, DDRGs are radio sources with features of recurrent activity. The active nucleus has a jet activity cycle (Hunik and Jamrozy, 2016). A jet activity may undergo another cycle after completing the first cycle in fading structures. This causes the emission to break again, and the spectrum of the new radio core getting even flatter as compared to that of the diffuse regions. Radio sources with recurrent activity such as J0840+2949, J1835+6204 and others features steep radio lobes and an active radio core (Saikia, 2010).

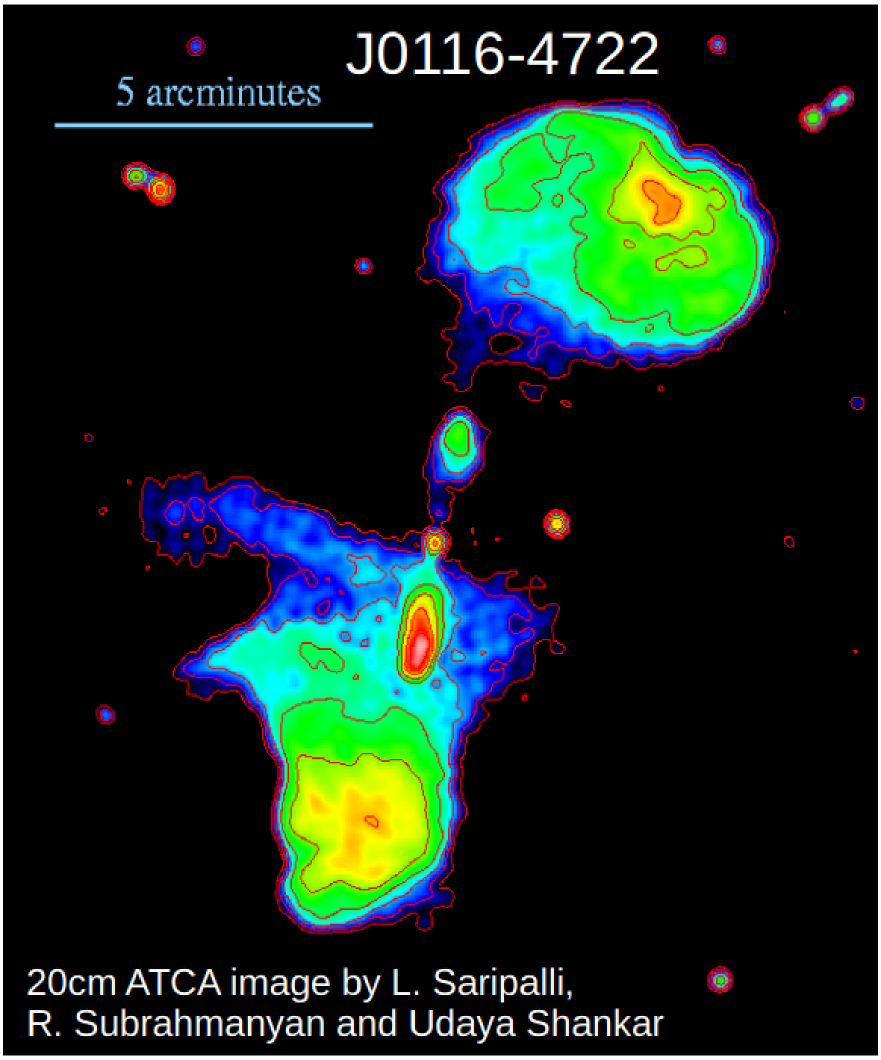

Figure 2.4: Double-double radio galaxy structure of J0116-4722 (Saripalli *et al.*, 2003).

2.2.2 Spectral Ageing of Radio Galaxies

The most interesting way of studying the history of RGs is through their morphology and spectral distribution of the radio lobes. Understanding the life cycle, and the consequences they have on the outer environment is essential in the understanding of source formation. Spectral ageing has been found to be a most useful mechanism used in determining the time scale of the radio sources (Mahatma, 2017). This mechanism helps in determining the time it took for an electron within the radio lobes to emit its energy via synchrotron and inverse-Compton losses. The synchrotron emission re-position to higher frequencies and the spectrum of the radio lobes gets much steeper as the electrons radiate away. The precise time that the radio galaxy has been active can be determined from the spectral index of the aging electrons within the radio lobes. The epoch and the radio spectrum of the object relation was also utilised as another way of determining the time the radio galaxy has been active in the olden days (Mahatma, 2017).

The radiation flux, S, from the radio source follows a power-law distribution characteristic of synchrotron emission, $S_\nu \alpha \nu^\alpha$. The time at which the plasma was formed can be determined from α, which is flat at the edges of the radio sources, flattest in the hotspot regions, and get steeper towards the inner edge of the lobes. This is often compatible with high-speed jets transporting plasma from the center and forming relativistic electrons at a shock area. The movement of the shock leaves plasma behind in the lobe that loses energy and α steepens. The areas closer to the active nucleus loses energy and show steeper spectra since they were formed earlier. There are more detailed models which can be used for spectral ageing calculations/determinations, the two most widely used are the Jaffe-Perola (JP) model and Kardashev-Pacholczyk (KP) model (Jaffe and Perola, 1973).

2.3 UNIFICATION MODEL

AGNs were difficult to classify in the past due to some telescopes with poor resolutions. It is postulated that different classes of AGNs arise from different observing points (Krawczynski and Treister, 2013) where the active nucleus is a SMBH enclosed by an accretion disc, clouds of gas and a dusty torus (Middelberg, 2008). This is known as the unified model, which suggests that the classes of the objects briefly discussed in subsections of Section 2.1 essentially belong to the same class of objects and they only differ as the results of the viewing angles (Bianchi *et al.*, 2012). At high luminosities, the unification model suggests that in Seyfert I, Quasars and Blazars, for an example, the active nucleus is observed nearly directly. In Seyfert II and RGs, the nucleus is seen through the hidden structure which obstruct a straight field of vision of continuum, broad-line area. Figure 2.5 is a schematic drawing of an unified model showing different classes of AGN depending on the observing point.

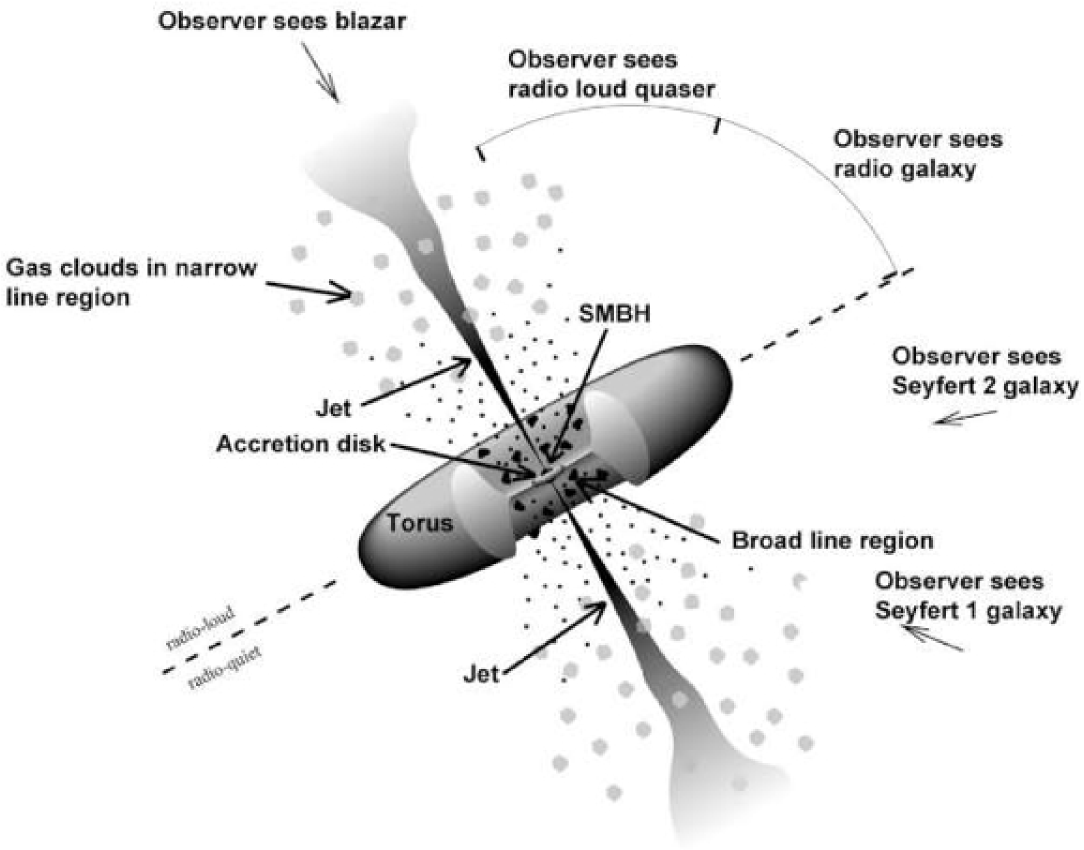

Figure 2.5: Unified model showing different classes of AGN when observer is observing from different angles. Credit: NASA

From the schematic unification model the active nucleus is enclosed by an optically dense 'dusty torus' regime. This dusty torus, where a thick molecular torus formed from the material in the host galaxy also blocks photons from the active nucleus. Depending on the viewing angle, some radiation can be blocked from viewer. A dust structure enclosing a compact nucleus has been spatially resolved by mid-infrared observations in NGC 1068 (Jaffe *et al.*, 2004). This gives some evidence for radiation not to be observed clearly because of being obscured by dusty tori. The difference in observations of Seyfert 1 and 2 galaxies can be justified by the dusty torus. The radio sources which have FR II radio morphology and radio loud quasars are viewed as similiar objects by the unification model, but it is not clear why some AGN have the FR I radio morphology while some have FR II.

2.4 GIANT RADIO GALAXIES

A RG that has evolved to massive size is called a GRG (Dabhade *et al.*, 2020*b*). The first GRG known as 3C 236 has an overall linear size of ∼4.95 Mpc and was discovered in 1974 (Andernach *et al.*, 2012). The GRG J1420-0545 is the largest known GRG to date with the overall linear size ∼4.95 Mpc (Machalski *et al.*, 2008).

2.4.1 Properties of Giant Radio Galaxies

GRGs are found to be different amongst the classes of extragalactic structures, which cover a scope of radio morphology, size, and structures. They have an overall projected linear sizes of 0.7 Mpc extending to 4.95 Mpc (Kuźmicz *et al.*, 2018), and also display FR II class morphology. Cause of their large sizes is a mystery but there are two hypotheses: (i) their huge structure is caused by the low density environments they reside in, and (ii) they are fuelled by the source central engine (Dabhade *et al.*, 2020*b*).

GRGs are very rare and not easily detected if the radio lobes have low surface brightness. This could be the case for the less luminous GRGs with huge overall projected linear sizes. The radio lobes of the extended radio sources may appear to be frail at higher redshifts, where the inverse-Compton losses against the cosmic microwave background radiation are large (Kuźmicz *et al.*, 2019). This might cause the compact sources or radio lobes to look disconnected from the active nucleus, making it difficult to detect the GRGs. To date only 348 GRGs have been confirmed (Kuźmicz *et al.*, 2019), and more of them are being discovered as a result of developing radio interferometers like the Murchison Widefield Array, the MeerKAT, and the Low-Frequency Array (Kuźmicz *et al.*, 2018).

Previous studies of GRGs focused on the properties of individual radio sources (Kuźmicz *et al.*, 2019), such as the huge size of radio structures. Based on research studies done previously, the ages of the GRGs in their sample are comparative to that of typical measured radio source, and they evolve in regions of low density, empowering them to evolve comparatively fast (Dabhade *et al.*, 2020*b*). The two aforementioned points regarding the age and the environment were experimented on massive consistent selected extended radio sources, but in small samples the outcomes are contradictory (Dabhade *et al.*, 2020*a*). The hypotheses that GRGs are the oldest RGs and had adequate time to grow to massive size contradict with the findings of Dabhade *et al.*, who have detailed that some extended radio sources grow in cluster environments (Dabhade *et al.*, 2020*b*). Because of their exceptionally large special features of lobes, GRGs are magnificent laboratories to study how the particle and magnetic field energy density evolves, and acceleration of high-energy cosmic rays. They can also be used in the studies of large-scale environments (Dabhade *et al.*, 2020*b*).

2.4.2 Formation and Evolution of Giant Radio Galaxies

Most studies of GRGs focus on understanding the massive physical scale and other properties of these objects. It is believed that the giant sources could be the end of a radio source's evolution. A radio source starts as a small source, and as the jets start to expand and feeds the radio lobes with pressure, the source changes to FR I or FR II radio galaxy. At some stage the jets stop and the electrons slowly start losing energy causing the radio power to decrease while the radio lobes continue to expand. The P-D diagram (see Figure 2.6) was developed to investigate the growth of the massive radio sources Dabhade *et al.* (2017).

This diagram indicates that massive radio sources have low luminosity at 1.4 GHz, which could result from the decrease in luminosity as these radio galaxies evolve. From the evolutionary models the radio lobes become less bright as the structure evolves to a huge size after an initial rapid increment (Dabhade *et al.*, 2017). The absence of radio sources in the top right corner of the diagram, suggests that the radio sources are evolving towards lower power and massive as they become older. The P-D diagram also indicates a cutoff in the GRG radio power at $\sim 10^{26}$ W Hz^{-1} with an extreme decrease in linear size exceeding 3 Mpc.

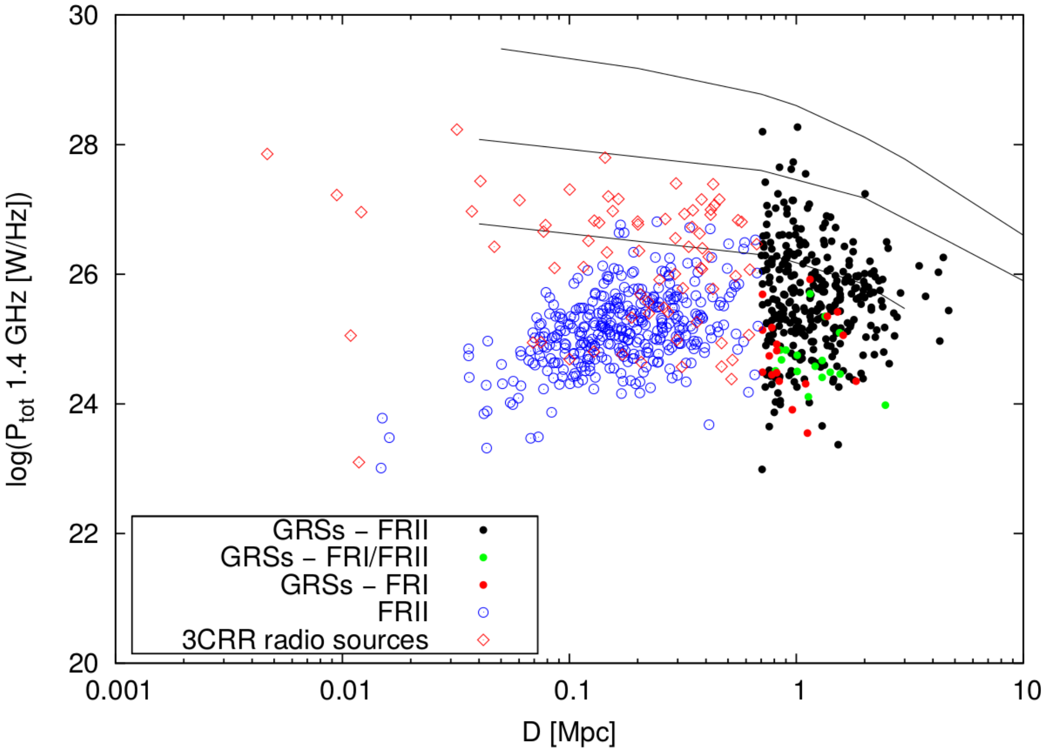

Figure 2.6: P-D diagram for FRII GRSs (black dots), FRI/FRII GRSs (green dots), FRI (red dots), 3C Radio Galaxy Catalog (red diamonds) (Laing *et al.*, 1983), and FRII radio sources (blue circles) (Kozieł-Wierzbowska *et al.*, 2020). The solid lines are the evolutionary scenarios for jet powers from Kaiser *et al.* 1.3×10^{40} W at $z = 2$, 1.3×10^{39} W at $z = 0.5$, and 1.3×10^{38} W at $z = 0.2$ (Kuźmicz *et al.*, 2018).

2.5 GRG J0133-1303

GRG J0133-1303, the only extended radio source found in a KAT-7 field of the cluster of galaxies ACO209, was discovered at a frequency of 1.83 GHz using the KAT-7 array (Colafrancesco *et al.*, 2016). KAT-7 was built as a precursor to the 64-dish MeerKAT telescope near the Square Kilometre Array (SKA) core site in the Karoo area of the Northern Cape, South Africa (Foley *et al.*, 2016).

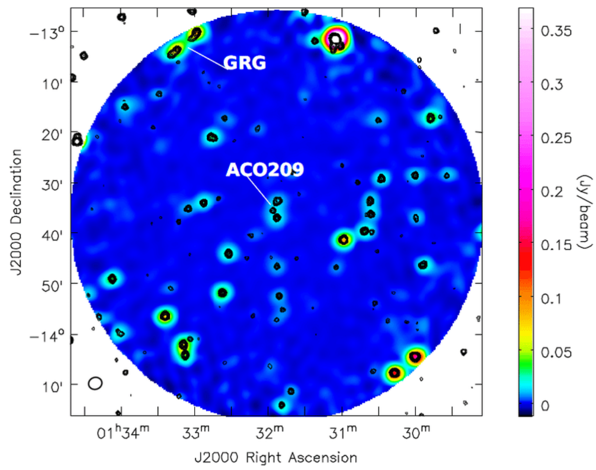

(a) KAT-7 image at 1.83 GHz

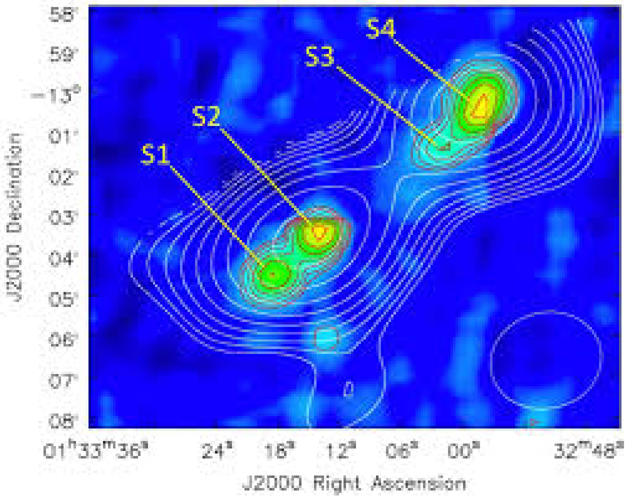

(b) GRG J013313.50-130330.5

Figure 2.7: Left: An image of the KAT-7 field of the cluster of galaxies ACO209. The radio source observed using KAT-7 at 1.83 GHz is labelled GRG at the top edge. Right:A zoom of the GRG with the NVSS contours (red) and KAT-7 contours (white) overlaid. (Colafrancesco *et al.*, 2016).

Previous studies have shown that GRG J0133-1303 shown in Figure 2.7a indicated by abbreviation GRG, has a core luminosity of $P_{1.4GHz} \approx 5.52 \text{ x } 10^{24}$ W Hz^{-1}, and luminosity $P_{1.4GHz} \approx 1.29 \text{ x } 10^{25}$ W Hz^{-1} and $P_{1.4GHz} \approx 0.46 \text{ x } 10^{25}$ W Hz^{-1} for the NW and SE lobe respectively, in agreement with the typical luminosities of GRGs (Colafrancesco *et al.*, 2016). Figure 2.7b shows the GRG with an extended emission resolved into two components and the NVSS has resolved the radio source into four components S1 (southern-east lobe), S2 (core) and S3 and S4 (northern-west lobe) which indicate an astrophysical link with the lobes and the compact core of an extended radio source. This clearly suggests that the extended emission uncovered using the KAT-7 telescope constitutes more than two components. Poor resolution of the KAT-7 radio telescope due to its small baselines and small collecting area could not resolve the source to its components in the northern lobe therefore, for deeper and detailed analysis there is a need for high resolution observations which were obtained from the GMRT.

2.6 GRG J2256-3617

The GRG J2256-3617 shown in Figure 2.8, was first observed in a radio survey in 1989 by the Automated Plate Measurement galaxy survey (Maddox *et al.*, 1990). The radio source has an overall projected linear size of $\sim$ 1.5 Mpc at redshift $z \approx 0.09$, and the core is observable in the Sydney University Molonglo Sky Survey (SUMSS) (Dabhade *et al.*, 2017). A compact region is observed in the northern lobe, while the southern lobe is scattered (Dabhade *et al.*, 2017). This compact regions are typical of hotspots observed in FR II (Fanaroff and Riley, 1974).

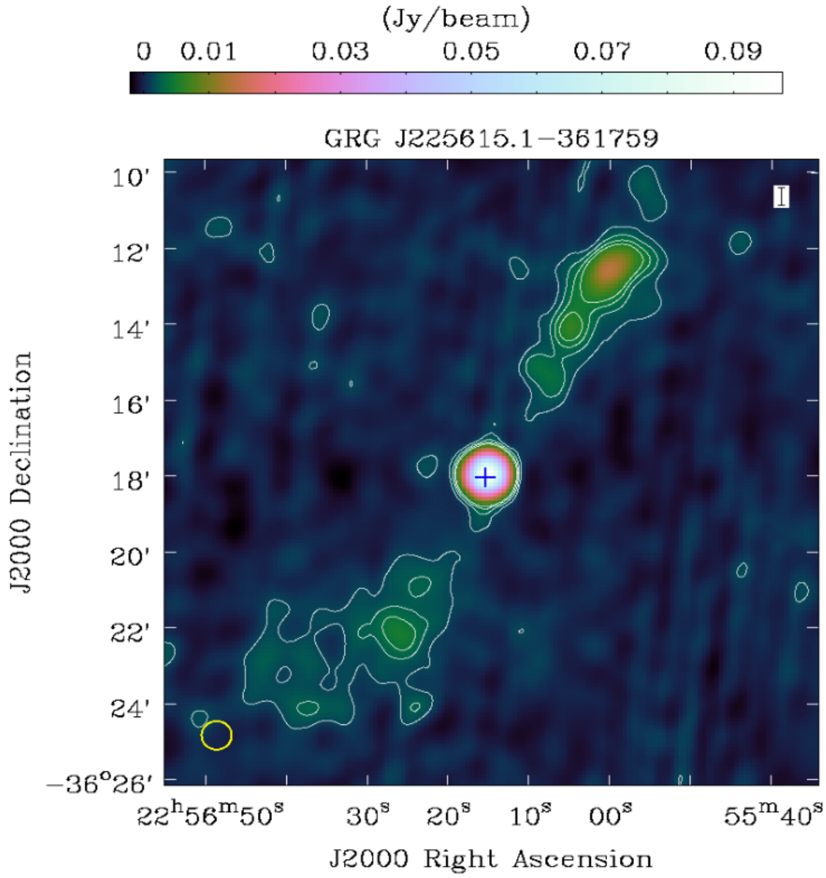

Figure 2.8: NVSS colour (Cube-Helix) and contour map of GRG J225615.1-361759. The NVSS beam represented in yellow at the bottom left corner. The core is marked with '+' symbol (Dabhade *et al.*, 2017).

CHAPTER 3

DATA ACQUISITION AND REDUCTION

This chapter is divided into two parts which illustrates the methodology followed throughout the research project. The detailed representation of the data observations and reduction are discussed in section 3.1, together with imaging and self-calibration to improve the quality of the image. Lastly, the description of different surveys used and also archival data from the respective websites is given in section 3.2.

3.1 THE DATA

Data from follow-up observations with the GMRT obtained at two different frequencies, i.e. 325 MHz and 610 MHz, were reduced and imaged using two different astronomical data reduction packages, Astronomical Image Processing System (AIPS) and Source Peeling and Atmospheric Modelling (SPAM). In addition to the GMRT data, we also used publicly available radio data from NRAO VLA Sky Survey (NVSS), SUMSS and Galactic and Extragalactic All Sky MWA (GLEAM) survey obtained via the Vizier website[1], VLA All Sky Survey (VLASS) survey was obtained from VLASS website[2] and KAT-7 obtained from Colafrancesco *et al.*. These archival data were used together with the data from the GMRT to compute the integrated spectra for the lobes and core of the radio sources.

3.1.1 GMRT Instrument

The GMRT, located 80 km north of the city of Pune in India is a sensitive radio telescope facility specializing at low frequency part of radio sky. This telescope is constituted of 30 dishes of 45m diameter. Twelve dishes form a random array in the middle, and other eighteen are equally dispersed along the three arms of an approximate 'Y' configuration, resulting in a highest baseline separation of about 25 km as shown in Figure 3.1 (Ananthakrishnan, 1995).

[1] http://vizier.u-strasbg.fr/viz-bin/VizieR
[2] https://science.nrao.edu/vlass/vlass-data

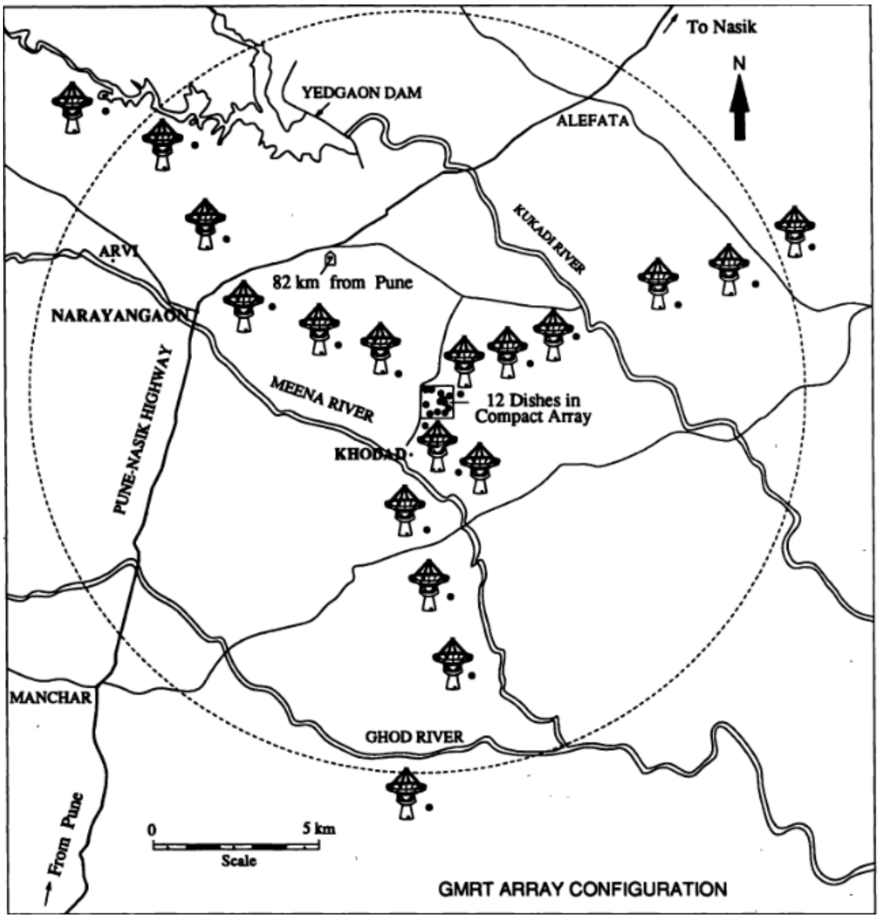

Figure 3.1: Antenna configuration of the GMRT with the dotted circles indicating the approximate size of the synthesized aperture (Kapahi and Ananthakrishnan, 1995).

3.1.2 GMRT Observations and Data Reduction

The full data of the GRG J0133-1303 were observed using the GMRT instrument at 2 different frequencies of 325 MHz and 610 MHz, while data from the second radio source J2256-3617 was obtained from the GMRT online archive[3]. Table 3.1 gives the detailed observations summary of the two radio sources.

[3]https://naps.ncra.tifr.res.in/goa/data/search

	J0133-1303	J2256-3617
Telescope	GMRT	GMRT
Antennas	27	28
Pointing Centre (RA, DEC)	01:33:10.0059, -13.01.59.963	22:56:15, -36.17.58
Observation date	2016 January	2014 August
Total observation time	4 hours	5 hours
Flux calibrator	3C147	3C48
Phase calibrator	0116-208	0116-208
Central frequency	0.3060 GHz	0.3060 GHz
*Bandwidth	33333.3320 KHz	-
Channels	512	256

Table 3.1: Detailed summary of GRG J0133-1303 and J2256-3617 observations.
*Bandwidth for GRG 2256-3617 is not available in literature and from SPAM pipeline output.

3.1.2.1 Data Reduction

Only data obtained from the GMRT at frequency of 325 MHz for GRG J0133-1303 were reduced (processed) using the National Radio Astronomy Observatory (NRAO) standard calibration task in AIPS packages. AIPS is a software package developed by NRAO, to support the reduction and analysis of data taken with radio telescopes (Palmer, 1996). The FITS file was loaded on AIPS using AIPS FITLD task. After the uv data were loaded they were indexed to allow speedy access of the data set. This was done using INDXR task setting CPARM(3)=1, for a time interval of one minute, and an NX table and a null calibration table (CL) were generated. LISTR task was used to print the list of scans and general information such as source names, frequency, duration, and scan structure. As the results of the first couple of visibilities of each of the scans are usually of poor quality or may have wrong time, the first few minutes data from each scans were flagged by running QUACK task over the whole data set with OPCODE and APARM(2) set as 'BEG' and 0.5 respectively.

The phase calibrator source 011-208 and flux density calibrator source 3C147 were used to calibrate the data which was flagged using QUACK task, in flux and phase. Prior further calibration, the flux density of the flux calibrator were accurately set. SETJY task was performed with the following parameter settings: OPCODE='CALC' and SOURCE='3C147' to control the flux densities of flux calibrator. CALIB task was used to secure the antenna dependent gain solutions. Before this task could be performed, CALSOUR was set to '3C147' and '0116-208'. The SOLINT which controls the solution interval in minutes over which the data are avaraged before solving for the antenna gains was set to 5 minutes, and SOLTYPE was set to default. Since the CALIB task was to give the gain solutions for amplitude and phase, the SOLMODE was set to A&P. The SN table was created to keep the determined antenna dependent complex gains. The GETJY task which determines flux source densities of the flux calibrators kept in the SU table, and the amplitude gain solutions kept in the SN table for the primary and secondary calibrators was used to get the flux density of 0116-208.

CLCAL which is used to manage SN and CL calibration tables was used to interpolate the antenna gain solutions of the target source obtained from the 3C147, 0116-208 and J0133-1303. The OPCODE parameter was set to CALI. This consolidates the selected good solution tables, and applies them to the old CL table that was created from INDXR task in order for the gain solutions to be incrementally enhanced. The outcomes of the interpolated solutions were stored in the higher versions of CL table. The SOURCE parameter was set to '3C147', '0116-208' and 'J0133-1303', CALSOUR to '3C147' and '0116-208' and INTERPOL to default. The afore-mentioned 3 tasks (SETJY, CALIB and CLCAL) were done repeatedly every time after running TVFLG task to remove bad data, which resulted from the Radio Frequency Interference (RFI) and antenna malfunctions. More flagging was done using UVFLG and WIPER tasks. Prior to the editing of the data set to remove the poor quality for further analysis, the data set were displayed using UVPLT task to identify bad data. Similarly, the VPLOT task was used to plot individual baselines.

This was followed by the bandpass calibration in order to detect the accurate measurement of spectral features. To perform bandpass calibration the flux density calibrator source 3C147 was used. The bandpass calibrator is considered to be a strong point source with sustained flux density covering the entire spectrum so that the complex gain variation of the antenna as a function of spectral channels is revealed. Most of the residual complex gain errors covering the entire spectrum resulted from the antenna based bandpass response functions which can be factorised into antenna based bandpass. This was achieved by setting the BPASS parameter option BPASSPRM(10)=2. The BPASS task generate a Bandpass (BP) table to store the antenna depended bandpass response function in bandpass table attached with the uv-dataset. The antenna dependant bandpass solutions for each polarization (RR or LL) stored in the BP table were checked using the POSS task with the option APARM(8)=2 . Also, the baseline cross-power spectrum for each polarisation were checked by applying the gain calibration from the CL table and the bandpass corrections from the BP table using the POSS option DOBAND=1.

The SPLIT task was used to divide the multi-source uv data into separate sources. The selected gain calibration table was applied to the 'J0133-1303', which is the target source data, by setting the parameters DOCALIB=1 and GAINUSE=2. The task applies the calibration directly to the visibilities on 'J0133-1303' and created a single source UV-data file and avaraged 512 channels to 16 channels at 325 MHz. Furthermore, the CLIP task was used to flag the RFI that affected the flux and phase calibrators. The CLIP task flags the RFI by searching for amplitudes that are out of range. For both calibrators, amplitudes that were above 7 Jy were clipped. To write the uv-data on FITS-tape the FITTP task was used. This was followed by a further flagging of the data using the IBLED task to get rid of the remaining RFI.

3.1.2.2 Imaging

AIPS task IMAGR was used to perform the Fourier transformation of the gain calibrated visibility data of J0133-1303. The J0133-1303 obtained from SPLIT task was used as input to the IMAGR task. The sky is non-polar at low radio frequency due to the wide primary field of view, therefore, 3D inversion was required. To correct the w-term effect the sky is divided into smaller portions, called FACETs. The adequate RA and DEC shifts for the center of the individual FACET, were produced in task IMAGR. This resulted in a 5×5 grid of FACETS, each of size 512× 512 pixels.

The 325 MHz maps were produced with the parameters: CELLSIZE=2x2, IMSIZE=0x0, NFIELD=49, NITER=10000000. The CELLSIZE is the pixel separation in arcsec, IMSIZE is the size of each field in pixels, NFIELD is the number of fields on the map in the antenna beam, DO3DIMAGE takes care of shifting the tangent point to each field center so that each field can be approximated as a 2D tangent plane to the celestial sphere, and the OVERLAP was set so that the strong source and its side lobes can be removed from the later overlapping fields before they are imaged. The maps were generated using different UV cut off. UVRANGE was used to specify the widths in U and V directions of the Gaussian function. The task IMAGR created two files, one is the beam file and the other being the map file. The target was field one of the map file.

3.1.2.3 Self Calibration

Calibrated visibilities were modified into radio image by making use of IMAGR task which carry out the self-calibration to reduce the antenna-based phase and amplitude RFI. Self-Calibration is performed to enhance the status of the image after carrying out the regular calibration process. Regular calibration entails taking random observations of a simple radio source of known structure to determine how the telescope responds to it. The calibration process is not accurate, as some RFI which can still be eliminated are left behind in the image. The RFI remain because the calibration source and the object under observation are in different parts of the sky, and as a result, the array is focusing at different parts of the ionosphere throughout the calibration and the observation. And again it is not possible to observe the calibrator continuously as this would leave no time to observe the object of interest. However, the ionosphere may alter a bit while the object of study is being focused.

After getting the first map, ten cycles of self-calibration were carried out using the task

CALIB. The following parameters were used in the task CALIB to carry out self-calibration: SOLMODE='P'; APARM(9) at default; NCOMP=1000000; NMAPS=25 and SOLINT = 17 for the first round. The SOLINT was adjusted by decreasing 3min for every cycle. Ten cycles of iterations of the task IMAGR and CALIB were carried out to obtain the final image. The FLATN task was used to rebuild the sky by combining the resulting set of facet images.

3.1.2.4 SPAM

To compare the integrated flux densities of various components from 325 MHz map produced using AIPS software, visibilities at frequency of 325 MHz and 610 MHz were processed for J0133-1303 and J2256-3617 data using the SPAM software package. SPAM is an addition to AIPS software package that provides semi-automated data reduction scripts for high-resolution, low-frequency radio interferometric observations at GMRT instrument (Intema, 2014). Beside its exceptional data reduction tasks, the software comprise direction dependent calibration and imaging, and different RFI and bad data mitigation tasks. The benefits of using the SPAM software on GMRT data: the data reductions are very efficient, highly reproducible, and give good quality results (Intema, 2014). The J0133-1303 and J2256-3617 data at 325 MHz and 610 MHz were reduced and calibrated using the SPAM pipeline[4]. The SPAM software was used to reduce 325 MHz and 610 MHz data because is non-coplanar, a wide field of view and also operate at low frequencies. Its peeling and ionospheric effects corrections using phase screens results in images with reduced artefacts. The SPAM package combines the raw data from the observations with the flag files and derives calibration and flags the data to create pre-calibrated visibility data. Before final image is produced, series of images are produced from pre-calibrated visibility with further flagging and calibration. Images produced from these software packages were used to compare the flux density of the core and the lobes with those obtained from the AIPS software package (see Chapter 4 for the results comparison). The images were also used to compute the integrated spectra, the spectral index map, and to study the morphology of the radio sources.

[4]http://www.intema.nl/doku.php?id=huibintemaspampipeline

3.2 ARCHIVAL DATA

Radio data for the two sources is also available in other surveys. The archival data in Table 3.2 and 3.3 were recorded from VizieR website. Vizier is used to query data at different wavebands. It also gives an access to the most complete library of published astronomical catalogues and data tables accessible online, and arranged in a self-documented database. To perform integrated spectra analysis we used data obtained from the GLEAM, NVSS, SUMSS, VLASS and TGSS surveys.

			Southern lobe & core *	Background source & northern lobe Ψ
Telescope	Beam Size/ Resolution(")	Frequency (MHz)	Flux Density (mJy)	
GLEAM	100	84	251.11±37.11	337.2±60.2
		92	229.134±33.86	299.1±51.1
		99	205.237±30.33	299.1±50.9
		107	254.409±37.59	266.6±38.3
		115	175.126±25.88	229.2±33.3
		122	187.68±27.73	254.2±30.9
		130	162.525±24.02	214.9±28.3
		143	176.98±26.15	259.7±31.5
		151	104.82±15.49	227.6±29.4
		158	153.95±22.75	175.4±27.7
		166	124.6±18.41	170.0±29.0
		174	162.312±23.98	190.1±27.8
		181	167.75±24.79	151.4±25.7
		189	107.488±15.88	165.7±25.0
		197	119.34±17.63	253.2±25.3
		200	116.1±17.16	186.1±96.77
		204	101.62±15.02	212.7±20.7
		212	92.257±13.63	195.1±20.0
		220	99.465±14.70	148.9±18.8
		227	106.79±15.78	128.8±19.7
KAT-7	180	1830	37.5±3.6	39.0±2.6

Table 3.2: Integrated flux densities together with respective uncertainties of GRG J0133-1303 at different frequencies from GLEAM and KAT-7.
* The core and southern lobe are merged into one blob.
Ψ The background source (B) and northern lobe are merged into one blob.

			Core	Northern Lobe	Southern Lobe
Telescope	Beam Size/ Resolution (")	Frequency (MHz)	Flux Density (mJy)		
GLEAM	100	76	228.408±76.23	410.698±87.435	554.528±107.075
		84	140.29±55.305	375.562±65.102	418.971±82.217
		92	199.019±44.668	357.665±53.869	395.427±69.898
		99	138.151±38.25	379.484±47.304	342.896±63.039
		107	181.475±33.824	374.495±43.364	350.748±59.888
		115	160.656±26.083	206.364±34.437	417.071±48.873
		122	148.1±23.903	238.489±32.492	386.917±47.306
		130	73.243±21.031	339.564±29.425	253.363±43.878
		143	162.305±14.743	288.532±21.784	343.599±33.872
		151	160.66±12.349	249.04±18.814	252.684±29.899
		158	145.959±11.765	245.431±22.823	298.365±21.784
		166	143.748±10.262	204.327±20.356	267.2±18.814
		174	140.817±11.214	233.881±23.956	313.392±22.823
		181	127.693±10.098	186.791±22.172	278.86±20.356
		189	175.778±9.506	185.812±21.346	261.201±23.956
		197	161.141±9.349	170.514±22.542	189.16±22.173
		200	163.073±88.06	198.485±88.06	245.689±141.654
		204	147.032±10.654	206.914±25.039	216.812±21.346
		212	193.292±11.799	183.072±29.831	266.789±22.542
		220	175.887±10.61	183.938±27.705	231.672±25.039
		227	167.879±44.963	225.008±31.353	193.248±44.963
TGSS	25	150	129.5±13.5	-	-
SUMSS	43	843	118.7±4.0	26.3±3.5	-
NVSS	45	1400	100.8±3.1	24.5±0.9	21.9±0.8

Table 3.3: Integrated flux densities together with respective uncertainties of GRG J2256-3617 for the core and lobes at different frequencies from GLEAM, TGSS, SUMSS and NVSS.

3.2.1 GLEAM

The GLEAM survey, with an angular resolution of 100 arcsec observed the entire sky south of declination (Dec)+30° between 2013 and 2015 from 72 to 231 MHz (Hurley-Walker *et al.*, 2019). Due to its large primary beam size some sky in the north $\delta > +25°$ is available with reduced sensitivity in the mid and lower parts of the GLEAM frequency range (Wayth *et al.*, 2015). The GLEAM was established to make data available for science objectives, which includes studying the active galactic nuclei and radio sources; diffuse galactic emission and the Galactic magnetic field; galaxy clusters; extragalactic and galactic spectral lines; supernova remnants; the Magellanic clouds; Galactic H II regions; cosmic rays: and pulsars and pulsar wind nebulae (Wayth *et al.*, 2015).

3.2.2 NVSS

The NVSS, which covers the sky north of J2000.0 $\delta = -40°$ (82% of the celestial sphere) was conducted at a frequency of 1400 MHz using the compact D and DnC configurations of the VLA from September 1993 to October 1996 to produce continuum and linear-polarization images with angular resolution of 45 arcsec, typical noise levels that are less than 0.5 mJy/beam and a point source flux density limit of about 2.5 mJy (George and Stevens, 2008). The compact core consisting of 27 radio telescopes is best for investigating the extended emission at 1400 MHz (Condon *et al.*, 1998).

3.2.3 SUMSS

The SUMSS (Mauch *et al.*, 2006) is a radio imaging survey at 843 MHz of the entire sky south of declination -30°. This survey has a resolution of 43" x 43" cosec $|\delta|$ and an rms noise level of $\sim$ 1 mJy/beam (Sadler and Hunstead, 2002). SUMSS also has similar sensitivity and resolution to NVSS and covers parts of the sky unaccessible to northern telescopes. The sensitivity of this telescope towards radio sources of large angular size and low radio surface brightness makes it well-suited to the detection of GRGs (Sadler and Hunstead, 2002).

3.2.4 VLASS

VLASS maps the sky at $\delta > -40°$, covering a total of 33,885 square degrees, with 2.5 arcsec angular resolution using the VLA B-array at 2–4 GHz, with an expected rms of 69 µJy/beam in the final images (Murphy, 2016).

3.2.5 TGSS

The TIFR GMRT Sky Survey (TGSS) ADR1 aimed at producing a reliable compact source survey is an imaging survey of the 150 MHz radio sky, using the GMRT (Intema *et al.*, 2016). Most of the pointing images from the survey have an approximate resolution of 25 arcsec and the rms noise level less than 5 mJy/beam (Intema *et al.*, 2016).

CHAPTER 4

GRG J013-1303

The GRG J0133-1303 maps were produced using AIPS software at 325 MHz only and SPAM software at both 325 MHz and 610 MHz. With the sensitivity of the GMRT, the GRG was detected with its core and the lobes. The integrated flux densities of various components from the map produced using AIPS software at 325 MHz will be compared with the ones from the maps produced using SPAM software at 325 MHz and 610 MHz. The integrated flux densities of the core and the lobes together with the uncertainties determined were also used to produce integrated spectra plots. The projected separation between the lobes and the core were determined using CASA software tools, as well as the angular size of the lobes and of the overall GRG. The spectral index map was computed from the uv tapered maps produced using the SPAM software at 325 MHz and 610 MHz map. The spectral index of various components were determine from the resulting map.

4.1 RESULTS

4.1.1 Morphology

Images at 325 MHz and 610 MHz from the GMRT data are presented in Figure 4.1, 4.2 and 4.3, respectively. Figure 4.1 was produced using AIPS software at 325 MHz only, while the images in Figure 4.2 and 4.3 were produced using SPAM pipeline at 325 MHz and 610 MHz. The images confirm the FR II radio morphology of GRG J0133-1303 presented and studied by Colafrancesco *et al.*. The KAT-7 telescope uncovered the extended emission into two components S1 (southern lobe), S3 and S4 (northern lobe), and S2 being the core of the GRG (Colafrancesco *et al.*, 2016). In their paper, there is no indication of compact structures. The core and the lobes of GRG J0133-1303 are not found in Parkes MIT NRAO, SUMSS, and TIFR GMRT Sky Survey.

The GMRT resolved the GRG into six components, southern lobe, the core, and the northern lobe is resolved into four components. The S1 and S2 which appears as southern-east lobe merged with the core in Colafrancesco *et al.* have been resolved into the southern lobe (S1) and the core (S2) in the GMRT map. The integrated flux density of the various components were measured using AIPS task TVSTAT (extended structures), and CASA task IMFIT (point sources). From the 325 MHz map computed using AIPS software the northern lobe is brighter than the southern lobe with the integrated flux density of 108.49 ± 5.21 mJy, while southern lobe has integrated flux density of 65.05 ± 3.27 mJy, and the integrated flux density of the core is 7.80 ± 1.40 mJy.

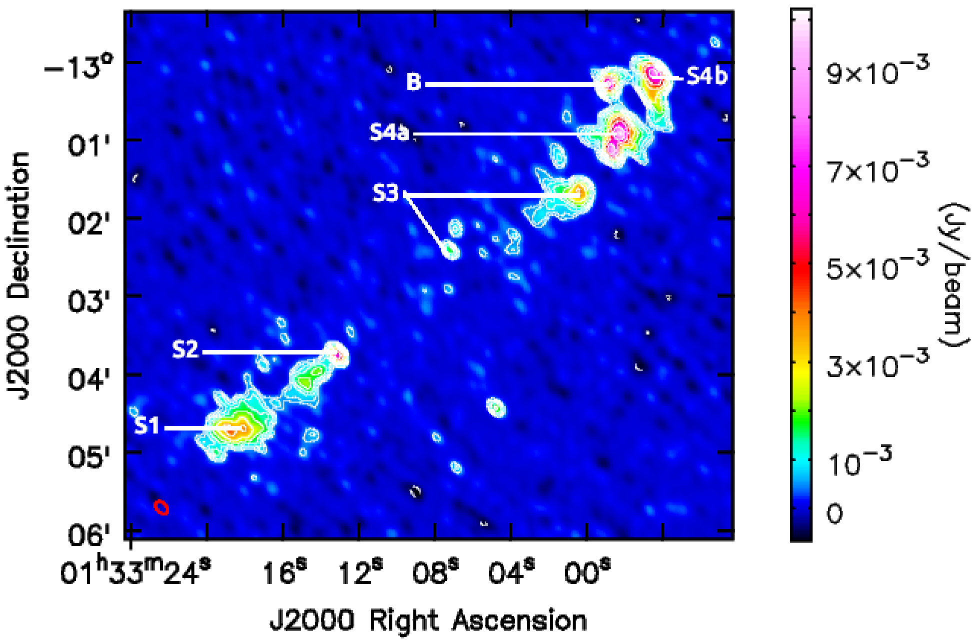

Figure 4.1: The 325 MHz GMRT image with contours overlaid starting from 3σ (σ = 0.16 mJy beam^{-1}) with $\sigma\sqrt{2}$ increments. The beam size of 11" x 7", represented in red at the bottom left corner of the image.

From the 325 MHz map produced using SPAM pipeline, the northern lobe is also brighter than the southern lobe with the integrated flux density of 113.18 ± 3.78 mJy, while the southern lobe has integrated flux density of 63.05 ± 3.17 mJy, and the integrated flux density of the core is 7.40 ± 0.63 mJy. The measured flux densities of the three components from 325

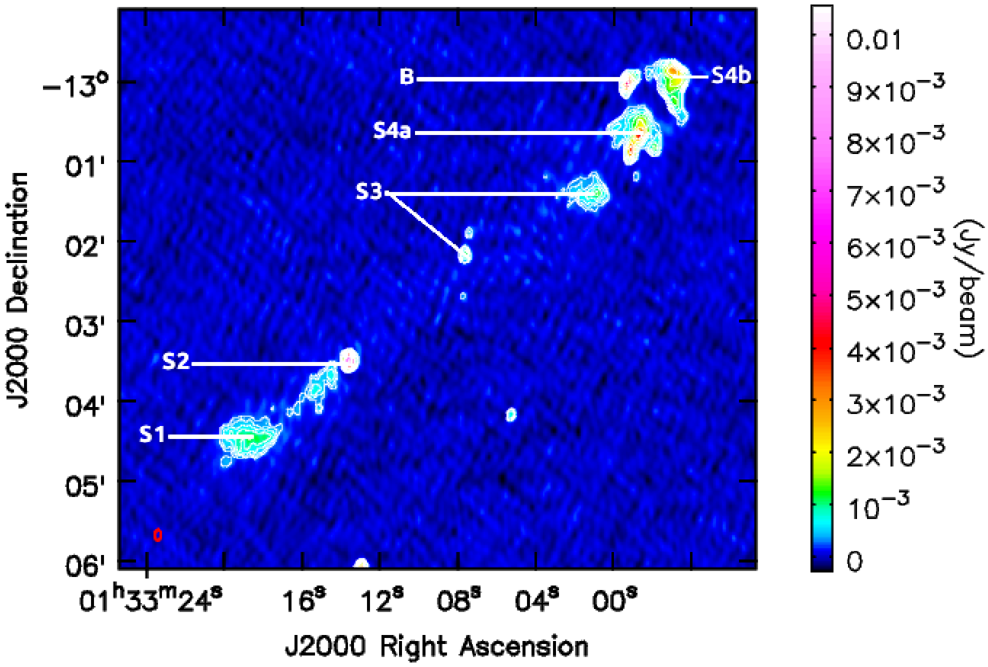

Figure 4.2: The 610 MHz GMRT image overlaid with contours starting from 3σ ($\sigma = 0.10$ mJy beam^{-1}) with $\sigma\sqrt{2}$ increments. The beam size of 10" x 6", represented in red at the bottom left corner of the image.

MHz map produced using SPAM pipeline are slightly close to the 325 MHz map produced using AIPS software.

The radio source at 610 MHz, also computed using the SPAM pipeline appears to have the same morphology as that of 325 MHz produced using AIPS software and SPAM pipeline. However, in 610 MHz image the core is brighter with the flux density of 11.97 ± 0.23 mJy. The northern lobe has an integrated flux density of 66.97 ± 3.01 mJy, while the southern lobe has integrated flux density of 46.34 ± 2.33 mJy. The uncertainties of the flux density were computed using:

$$\sigma_{s_\nu} = \sqrt{(S_\nu \sigma_{cal})^2 + \left(\sigma_{rms}\sqrt{\frac{area}{Beam}}\right)^2} \tag{4.1}$$

where σ_{cal} is the uncertainty in the calibration of the flux scale, S_ν is the integrated flux density at the observed frequency ν, σ_{rms} is the rms of the map, and σ_{cal} is taken to be 5

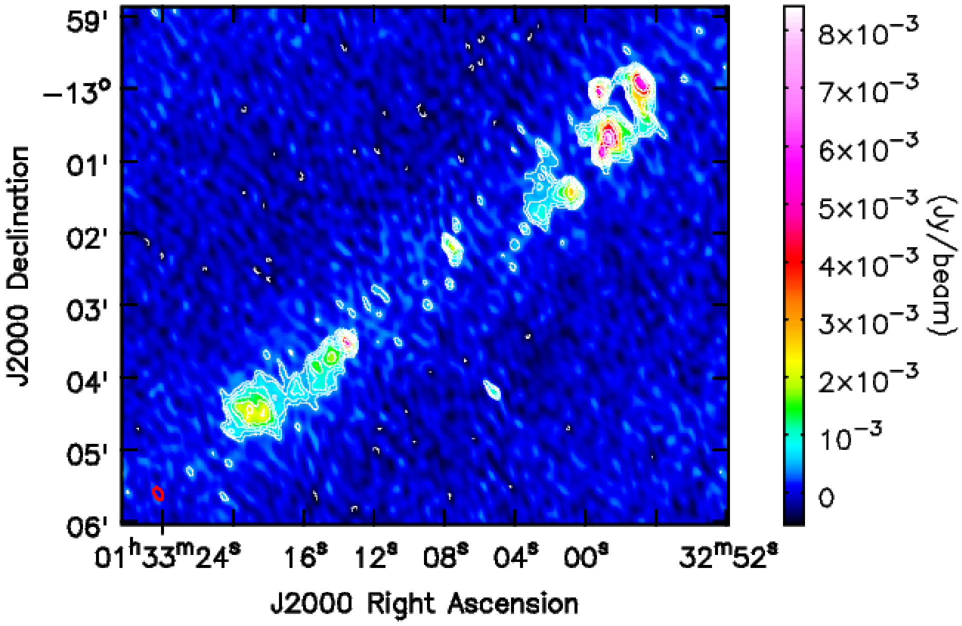

Figure 4.3: The 325 MHz GMRT image overlaid with contours starting from 3σ (σ = 0.14 mJy beam^{-1}) with $\sigma\sqrt{2}$ increments. The beam size of 8" x 4", represented in red at the bottom left corner of the image.

per cent for the GMRT. The area refers to the area of the source in pixels and the Beam is the number of beams that can fit within the area of source also in pixels. The measured flux densities and uncertainties of the core and the lobes are listed in Table 4.1. The northern lobe is measured to be ∼1.43 Mpc away from the core, while the southern is ∼0.47 Mpc away.

	Core	Background Source	Northern Lobe	Southern Lobe
Frequency (MHz)		Flux Density (mJy)		
325 AIPS	7.80±1.4	12.76±0.85	108.49±5.21	65.05±3.27
325 SPAM	7.40±0.63	13.6±2.40	113.18±3.76	63.05±3.17
610 SPAM	11.97±0.23	8.59±0.79	75.56±3.01	46.34±2.33

Table 4.1: Integrated flux densities together with respective uncertainties of GRG J0133-1303 for the Core, Background source (B), Northern lobe, and Southern lobe at 325 and 610 MHz.

Figure 4.4 represents a zoomed northern lobe, while Figure 4.5 represents a zoomed southern lobe and the core. The southern lobe is resolved into four components S3, S4a, S4b and B. The three components above S3 looks familiar to Narrow-angle tailed (NAT) source with the background source (B) being the possible core, and the S4a and S4b could be its lobes. The measured flux densities and the uncertainties of the four aforementioned components are listed in Table 4.2.

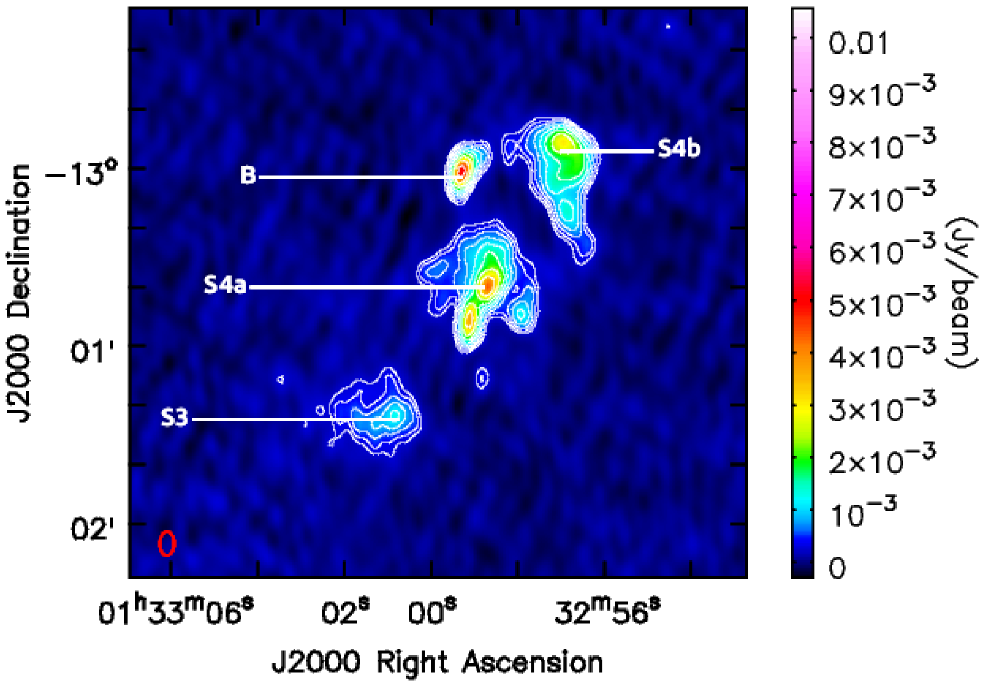

Figure 4.4: A zoom of the northern lobe at 610 MHz GMRT image with 610 MHz image contours overlaid starting from 3σ ($\sigma = 0.10$ mJy beam^{-1}) with $\sigma\sqrt{2}$ increments. The beam size of 10" x 6", represented in red at the bottom left corner of the image.

	S3	S4a	S4b
Frequency (MHz)	Flux Density (mJy)		
325 AIPS	21.95±1.10	53.62±2.68	35.67±1.78
325 SPAM	23.99±1.48	41.24±2.06	29.56±1.20
610 SPAM	13.43±0.67	31.32±1.57	22.15±1.11

Table 4.2: Integrated flux densities together with respective uncertainties of GRG J0133-1303 for S3, S4a, and S4b at 325 and 610 MHz.

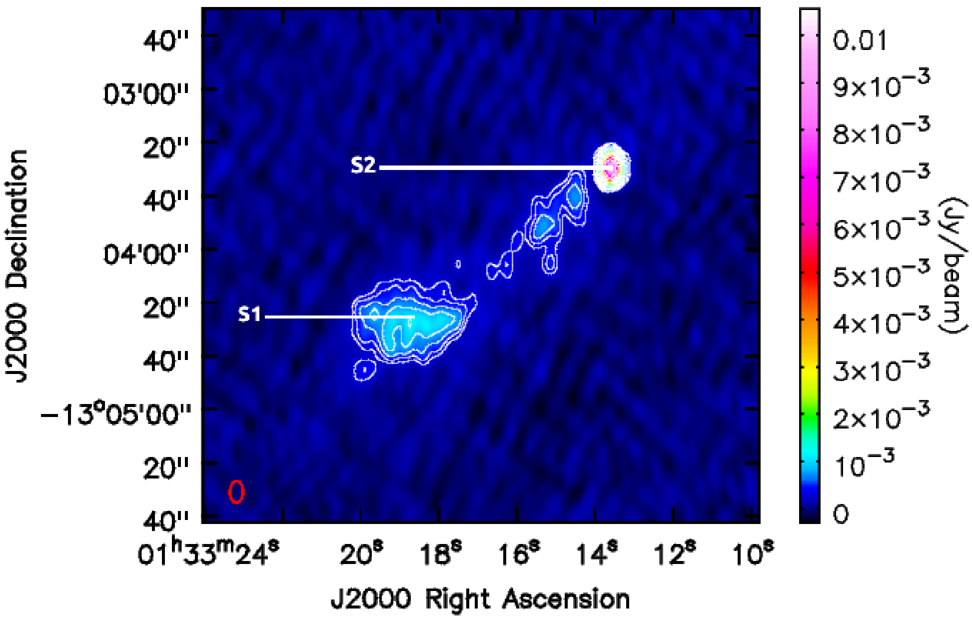

Figure 4.5: A zoom of the southern lobe at 610 MHz GMRT image with 610 MHz image contours overlaid starting from 3σ ($\sigma = 0.10$ mJy beam^{-1}) with $\sigma\sqrt{2}$ increments. The beam size of 10" x 6", represented in red at the bottom left corner of the image.

4.1.2 Multi-frequency Analysis

Figure 4.6 shows the ESO-DSS2-red[1] optical image of GRG J0133-1303 with the GMRT 610 MHz contours overlayed. The optical core has an angular size of ∼0.09 arcmin corresponding to the projected size of ∼0.03 Mpc and coincide with the core of the radio source. The projected separation between the cores is 0.03 arcseconds. The core of the radio source is also associated with the core of Wide-field Infrared Survey Explorer object J013313.50-130330.5, NVSS source S2, and the ROSAT X-ray source 1RXSJ0133138-13031. The GRG J0133-1303 has an angular size of ∼12.96 arcmin corresponding to the overall projected size of 3.59 Mpc at redshift $z \approx 0.3$. The northern lobe (excluding source B), starting from the bottom of S3 to the top edge of S4b, has an angular size of ∼3.95 arcmin, corresponding to the projected size of ∼1.1 Mpc, while the southern lobe has an angular size of ∼1.2 arcmin, corresponding to the projected size of ∼0.3 Mpc. The background (B) source of the optical source has angular size of ∼5.03 arcseconds and coincide with the background source of the

[1]https://archive.eso.org/dss/dss

radio source indicated in green box at top edge of the northern lobe but its redshift is not known.

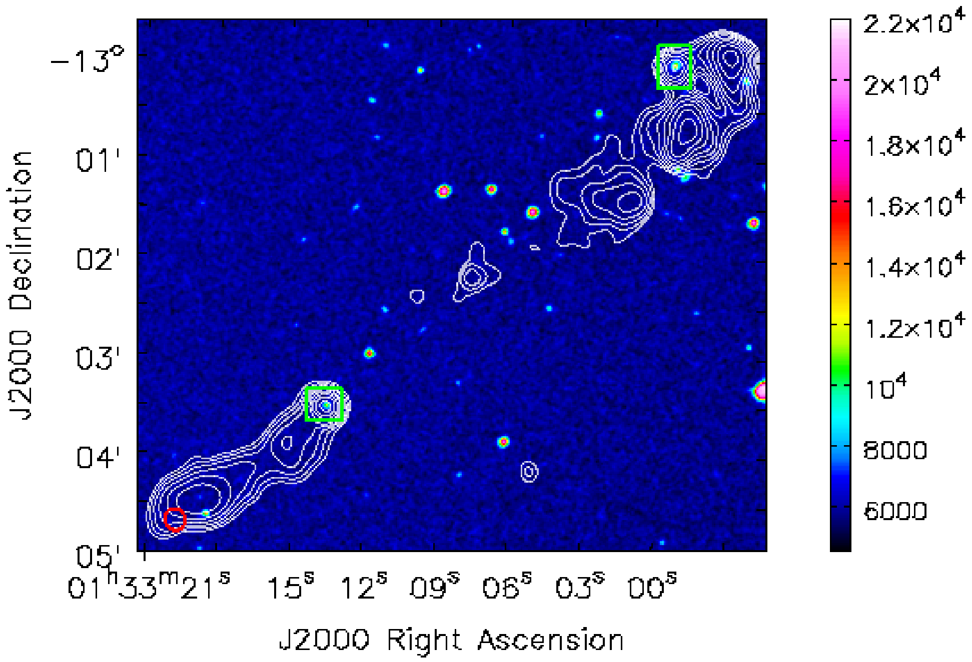

Figure 4.6: Contours of 610 MHz image overlaid on the DSS2-red optical map of GRG J0133-1303 starting from 3σ ($\sigma = 0.21$ mJy beam^{-1}) with $\sigma\sqrt{2}$ increments. The GMRT 610 beam size 13" x 13" is represented in red at the bottom left corner of the image.The core is indicated in the green box, and the units of the map are given in arcseconds.

4.1.3 Integrated Spectra

The flux density scaling was performed to check if the target follows the spectral distribution as the other sources in the image. The flux scaling factor was determined by comparing the integrated fluxes of three strong point sources selected from the GMRT at 610 MHz map with their counterparts in the GMRT at 325 MHz, GLEAM, and NVSS survey. The flux scaling factor was determined by taking the average of the ratios of the measured integrated flux densities of the three point sources from the GMRT map at 610 MHz and their predicted counterparts in the GMRT at 325 MHz, GLEAM surveys, and the NVSS. Both the GMRT maps at 325 MHz and 610 MHz were multiplied by flux scaling factor of 0.99. Furthermore, the position coordinates of these three point sources were used to perform a position correction on 325 MHz maps computed from AIPS and SPAM software. This was done in order for the sources on both 325 MHz maps to coincide with those of 610 MHz.

Figure 4.7 is the plot of the five-point spectrum of the core region. The core is merged with the southern lobe in GLEAM and KAT-7 image, hence, the flux densities from a core region in VLASS at 3000 MHz, NVSS at 1400 MHz, and the GMRT at 610 NHz and 325 MHz maps were measured, and the data was used to fit the quadratic function. The resulting function log[S/mJy] = -0.51(log[ν/MHz])^2 + 3.57log[ν/MHz] - 4.87 was used to predict the accurate GLEAM and KAT-7 fluxes for the core by substituting for KAT-7 at 1830 MHz and GLEAM frequencies in the curve. There is expectation for turnover due to synchrotron self absorption as it is usually expected for a compact core of AGN. The GLEAM and KAT-7 flux densities determined using the quadratic function were then subtracted from the total flux densities listed in Table 3.2, Section 3.2 to get the flux densities of the southern lobe at KAT-7 and GLEAM frequencies. The uncertainties of the flux densities were computed using:

$$\sigma_{s_\nu} = S_\nu \sqrt{\left(\frac{\sigma_1}{S_1}\right)^2 + \left(\frac{\sigma_2}{S_2}\right)^2} \tag{4.2}$$

where σ_1, σ_2 are the uncertainties of the flux densities, S_1, S_2 and S_ν are integrated flux densities.

The plot shown in Figure 4.8 is a four-point spectrum of the background source. The flux density from the background region in VLASS at 3000 MHz and the GMRT at 325 MHz and 610 MHz map were also measured and the data was used to fit the linear function. The resulting function log[S/mJy] = 2.23 - 0.45log[ν/MHz] was used to predict the accurate GLEAM and KAT-7 fluxes for the background (B) source by substituting for KAT-7 at 1830 MHz and GLEAM frequencies in the straight line. The background spectrum appears to be steep. The background source is merged with the northern lobe in the KAT-7, GLEAM and NVSS image. The same steps used to predict the accurate GLEAM and KAT-7 flux densities for the core were followed to determine the accurate flux densities for the background source and the northern lobe from KAT-7 at 1830 MHz, GLEAM at different frequencies and NVSS at 1400 MHz. In Table 4.3 we list the calculated flux densities, while the integrated spectra of the northern and southern lobe were then computed and are shown in Figure 4.9 and 4.10. From the plots, the spectral index for northern lobe is estimated to be α = -0.75±0.02, while for the southern lobe is α = -0.98±0.03

		Core	Northern Lobe	Southern Lobe	B
Telescope	Frequency (MHz)	Flux Density (mJy)			
GLEAM	84	1.30±0.025	314.08±58.07	249.81±37.08	23.12±2.13
	92	1.50±0.029	276.90±49.06	227.66±33.83	22.20±2.04
	99	1.68±0.03	277.62±48.92	203.56±30.30	21.48±1.98
	107	1.89±0.04	245.86±36.39	252.52±37.55	20.74±1.91
	115	2.10±0.04	209.12±31.45	173.02±25.84	20.08±1.85
	122	2.29±0.04	234.65±29.10	185.39±27.69	19.55±1.80
	130	2.51±0.05	195.90±26.55	160.02±23.97	18.99±1.75
	143	2.86±0.06	241.50±29.83	174.12±26.10	18.20±1.67
	151	3.09±0.06	209.84±27.77	101.74±15.43	17.76±1.63
	158	3.28±0.06	157.99±26.10	150.67±22.69	17.40±1.60
	166	3.50±0.07	152.98±27.44	121.10±18.34	17.02±1.57
	174	3.72±0.07	173.44±26.27	158.60±23.91	16.66±1.53
	181	3.76±0.07	135.03±24.20	163.99±24.90	16.37±1.51
	189	4.13±0.08	149.61±23.52	103.36±15.80	16.09±1.48
	197	4.35±0.08	237.44±23.85	114.99±17.55	15.76±1.45
	200	4.43±0.09	170.45±95.33	111.67±17.08	15.65±1.44
	204	4.55±0.09	197.19±19.27	97.07±14.93	15.51±1.43
	212	4.75±0.09	179.85±18.60	87.51±13.54	15.25±1.40
	220	4.96±0.10	133.91±17.42	94.50±14.61	14.99±1.38
	227	5.15±0.10	113.73±18.34	101.64±15.68	14.78±1.36
NVSS	1400	19.90±1.1	36.78±1.80	15.94±0.66	6.52±0.60
KAT-7	1830	22.42±0.43	33.22±2.07	15.08±3.17	5.78±0.53
VLASS	3000	21.60±0.31	-	-	4.81±0.46

Table 4.3: Integrated flux densities together with respective uncertainties of GRG J0133-1303 for the core and lobes at different frequencies from GLEAM, NVSS, kat-7 and VLASS.

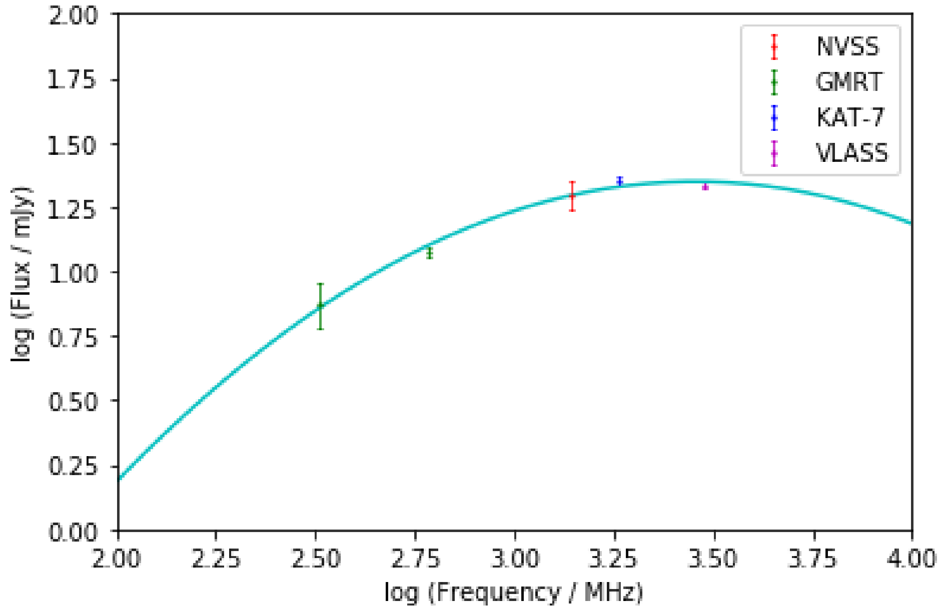

Figure 4.7: Integrated spectra of the core with blue line indicating the best-fit done using log[S/mJy] = -0.55(log[ν/MHz])^2 + 3.80log[ν/MHz] - 5.21

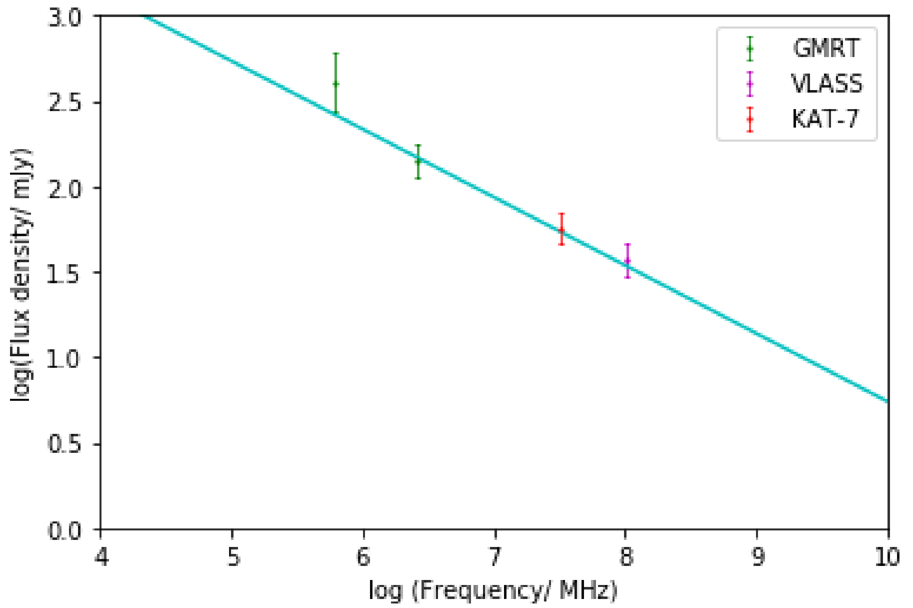

Figure 4.8: Integrated spectra of the background source with blue line indicating the best-fit done using log[S/mJy] = 4.72 - 0.40log[ν/MHz].

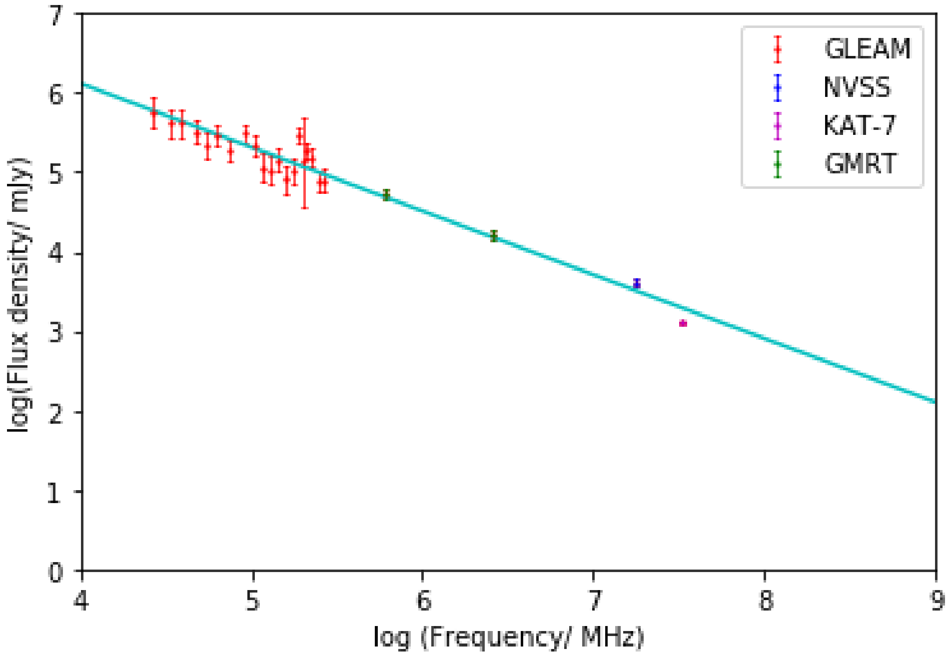

Figure 4.9: Integrated spectra of the northern lobe with blue line indicating the best-fit done using log[S/mJy] = 9.34 - 0.80log[ν/MHz].

4.1.4 Spectral Analysis

Spectra of the lobes of radio sources have given insight into remarkable characteristics and processes that determine their time scale (Mahatma, 2017). Figure 4.11 and 4.12 shows a UV-taper images produced using SPAM pipeline at 325 MHz and 610 MHz which were used to compute the spectral index image. The images were UV tapered to produce a circular beam of "13 x 13". In order to compute the spectral index map, the two maps had to be aligned so that the radio source on 610 MHz map coincide with that on 325 MHz map. The geometry of the maps were aligned using the HGEOM task in AIPS. The resulting image was used together with the 325 MHz image to compute a two-frequency radio spectral index image shown in Figure 4.13, using COMB task in AIPS. The spectral index values were measured using AIPS task TVSTAT for both the lobes and core. The following power-law form of the spectral index formula was used, $S_\nu \ \alpha \ \nu^\alpha$, where S is the radio flux density, ν is the frequency, and α is the spectral index. The uncertainties of the spectral index value

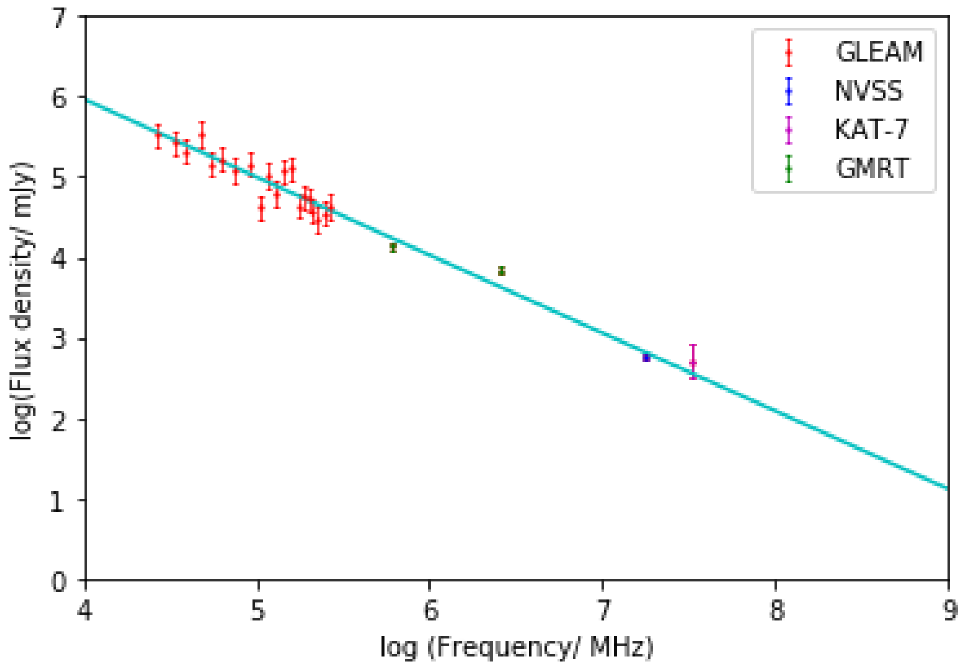

Figure 4.10: Integrated spectra of the southern lobe with blue line indicating the best-fit done using log[S/mJy] = 9.85 - 0.97log[ν/MHz].

were computed using:

$$\sigma_\alpha = \frac{1}{log\left(\frac{\nu_1}{\nu_2}\right) In(10)} \sqrt{\left(\frac{\sigma_1}{S_1}\right)^2 + \left(\frac{\sigma_2}{S_2}\right)^2} \tag{4.3}$$

where σ_1, σ_2 are the uncertainties of the flux densities, S_1, S_2 are the integrated flux densities at frequency ν_1, ν_2.

The spectral index of the extended radio source GRG J0133-1303 varies from $\sim \alpha = -0.7$ to $\alpha = 0.5$. The core has an average spectral index of $\alpha = 0.5 \pm 0.1$ which indicate a flat spectrum. The southern radio lobe has an average spectral index of $\alpha = -0.6 \pm 0.1$, while the northern lobe which is divided into four components has an average spectral index of $\alpha = -0.5 \pm 0.1$ (including S3, S4a and S4b). B has an average spectral index of $\alpha = -0.2 \pm 0.3$, S3 has an average spectral index of $\alpha = -0.7 \pm 0.1$ and S4a and S4b have an average spectral index of $\alpha = -0.5 \pm 0.1$, and $\alpha = -0.4 \pm 0.1$, respectively. The radio lobes have steeper spectral index when compared to the core which has flat spectral index, but flatter when

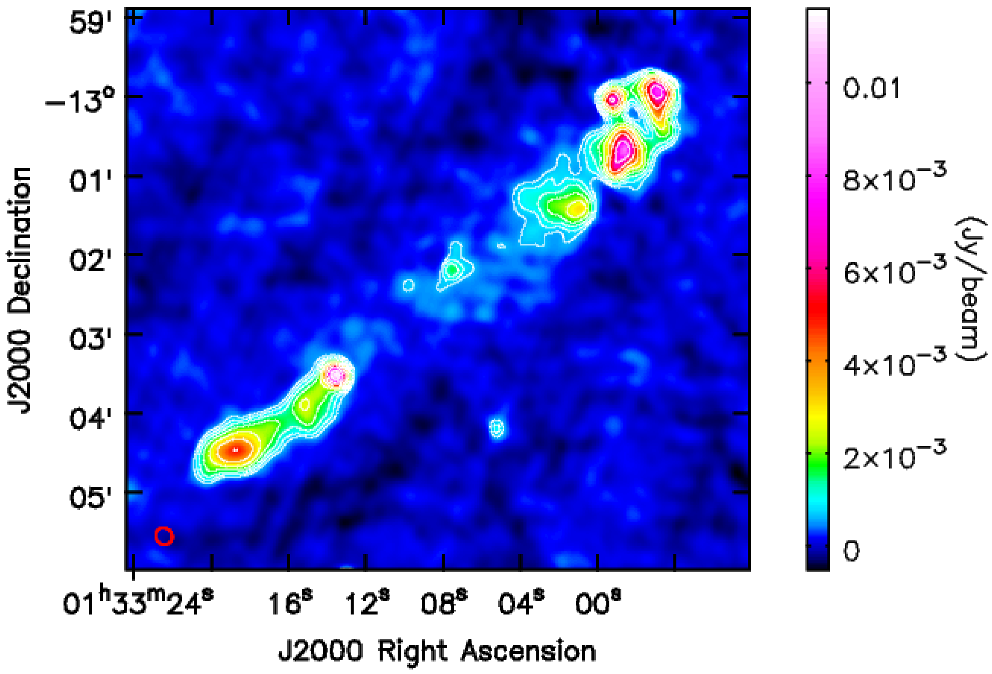

Figure 4.11: The 610 MHz UV-taper GMRT image with contours overlaid starting 3σ (σ = 0.28 mJy beam^{-1}) with $\sigma\sqrt{2}$ increments. The beam size of 13" x 13", represented in red at the bottom left corner of the image.

compared to other radio sources.

4.2 DISCUSSION

In this section the results of GRG J0133-1303 are being discussed as the main interest of this research report. The main objectives, and the two primary questions that this research study seek to address are as follows:

1. Search for the radio core, jets, lobes, and characterize the radio source.
2. Determine the type of radio morphology associated with the radio source.
3. Measure the projected size of the GRG.
4. Perform the spectral analysis of the radio source.
5. What type of radio morphology is associated with the radio source?

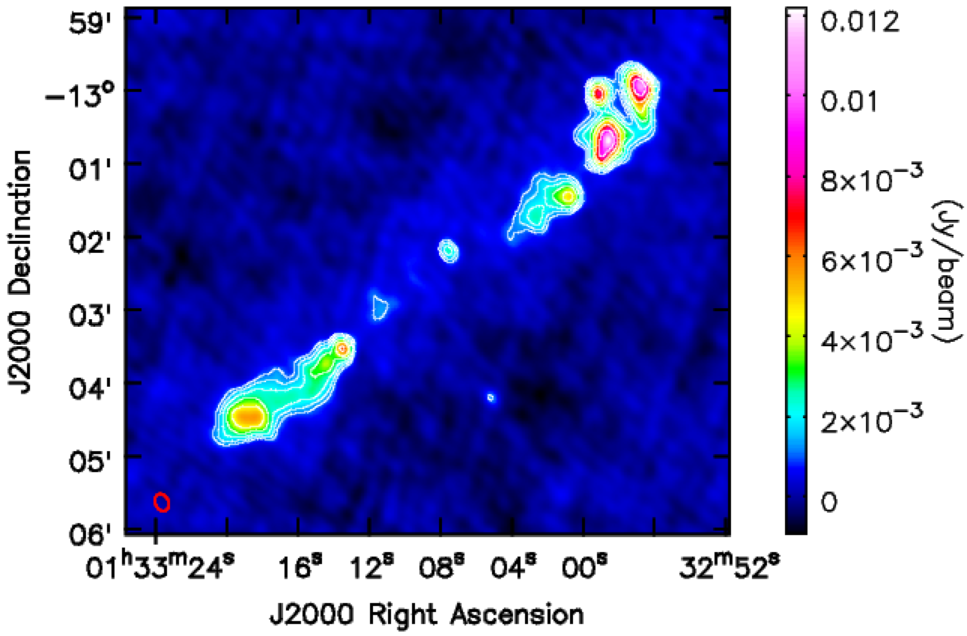

Figure 4.12: The 325 MHz UV-taper GMRT image with contours overlaid starting from 3σ (σ = 0.37 mJy beam^{-1}) with $\sigma\sqrt{2}$ increments. The beam size of 13" x 13", represented in red at the bottom left corner of the image.

6. What is the projected size of the GRG?

The GRG J0133-1303 display radio lobes that are axially symmetric, and bright, with an indication of FR II morphology. It is also interesting to notice that the northern lobe is divided into four components, with a compact source on the left side of the lobe. However, no jets and hotspots are detected. This suggest that there is no pressure being fed to the lobes, and/or the process that create the lobes is no longer active. This GRG has an overall projected size of ~3.59 Mpc at redshift $z \approx 0.3$, and the radio core coincide with the core of the optical source. The optical core has projected size of ~0.03 Mpc. The background source from the radio image also coincide with the background source from the optical source, however, its photometric redshift is not known. The northern lobe has a projected size of ~1.1 Mpc and it is ~ 1.43 Mpc away from the core, while the southern lobe has projected size of ~0.3 Mpc and it is ~ 0.47 Mpc away. Looking at the difference in projected separation between the northern lobe and the core, and between the southern lobe and the core, it is

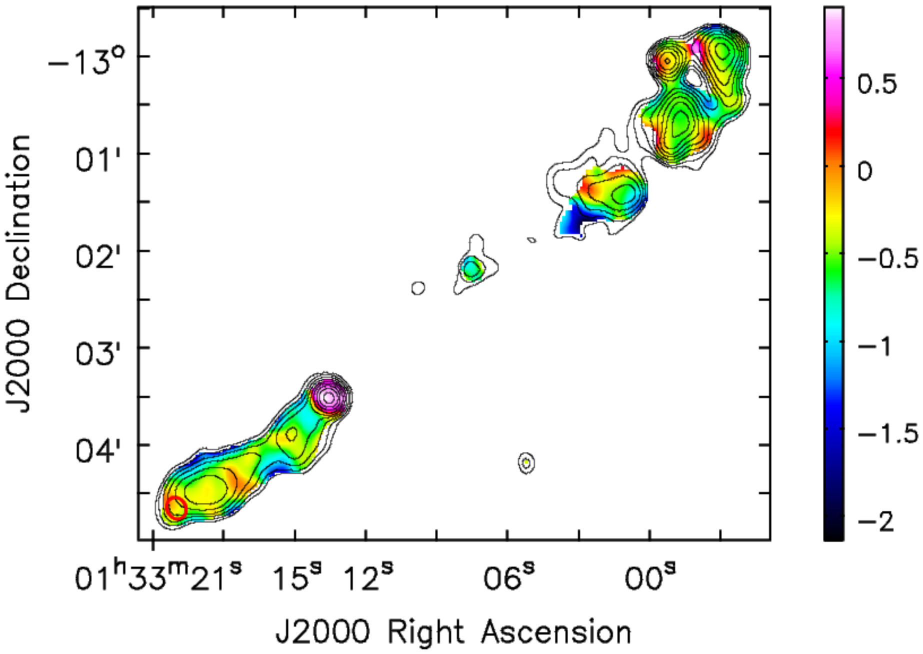

Figure 4.13: 325-610 MHz Spectral index map with 610 MHz GMRT UV-Taper image contours overlaid starting from 3σ (σ = 0.28 mJy beam^{-1}) with $\sigma\sqrt{2}$ increments. The beam size 13" x 13" represented in red at the bottom left corner of the image.

possible that the environments of the radio lobes are different suggesting that the IGM is relatively less dense in the northern lobe or it could be due to projection effects.

The Ned Wright cosmology calculator (Wright, 2006) was used to determine the luminosity distance (D_L) of the radio source. The radio power of the radio source was calculated using: (Dabhade *et al.*, 2017)

$$P_{1.4} = 4\pi D_L^2 S_{1.4} (1+z)^{\alpha-1} \tag{4.4}$$

where $S_{1.4}$ is the integrated flux density at 1.4 GHz, D_L is the luminosity distance, $(1+z)^{\alpha-1}$ is the k-correction determined from the cosmological calculator[2] for the flat universe, and α is the spectral index. At the photometric redshift of $z \approx 0.3$, the GRG J0133-1303 has radio

[2]https://home.fnal.gov/ gnedin/cc/

power of $P_{1.4GHz} \approx 0.16 \times 10^{24}$ W Hz^{-1}, which is compatible with the typical radio powers of the GRGs. The GRG J0133-1303 is indicated by a purple dot in Figure 4.14. This radio source falls among, and seems to be evolving the same way as other GRGs on the P-D diagram. From the diagram, the radio source has a low radio luminosity at 1.4 GHz frequency. This might suggest that as these radio sources evolve to Mpc scales, their radio luminosity decrease. The decrease in radio luminosity might be caused by the radiative energy losses and adiabatic expansion (Dabhade *et al.*, 2017). Supported by the evolutionary models, the luminosity of the radio lobes decrease at fast rate as the radio sources evolve to a massive size. The radio power of the radio sources decrease, and they evolve to massive size in low dense environment as they grow old. The radio core has luminosity of $P_{1.4GHz} \approx 6.08 \times 10^{24}$ W Hz^{-1}, while the northern and southern lobe has luminosity of $P_{1.4GHz} \approx 1.12 \times 10^{25}$ W Hz^{-1}, and $P_{1.4GHz} \approx 0.86 \times 10^{25}$ W Hz^{-1} derived using the source's luminosity distance of 1598.74 Mpc in the adopted cosmology.

From the spectral index map, the core appears to have a flat spectral index and also has an inverted spectrum, pointing at restarting nuclear activity. The radio lobe are steep most likely as the result of radiative aging, which causes the frequency break in the spectrum to shift to lower frequencies. This is probably because the electrons were formed earlier and are now suffering energy losses and ageing effects. This radio source is possibly starting a new cycle of nuclear activity, with the lobes probably being the remnants from the previous cycles since they are ageing. However, feeding of new material from the new cycle has not started since there is no indication of the inner or outer (double-double radio galaxies) lobes and the spectral index of the radio lobes are steep. Radio sources of this nature which have active radio cores and aging/dying lobes are called recurrent activity radio galaxies.

It is not clear if the three components B, S4a and S4b form part of the northern lobe or they could be a distinct sources. But reading from the spectral index map the southern lobe has an average spectral index of $\alpha = -0.6 \pm 0.1$, while S3 has an average spectral index

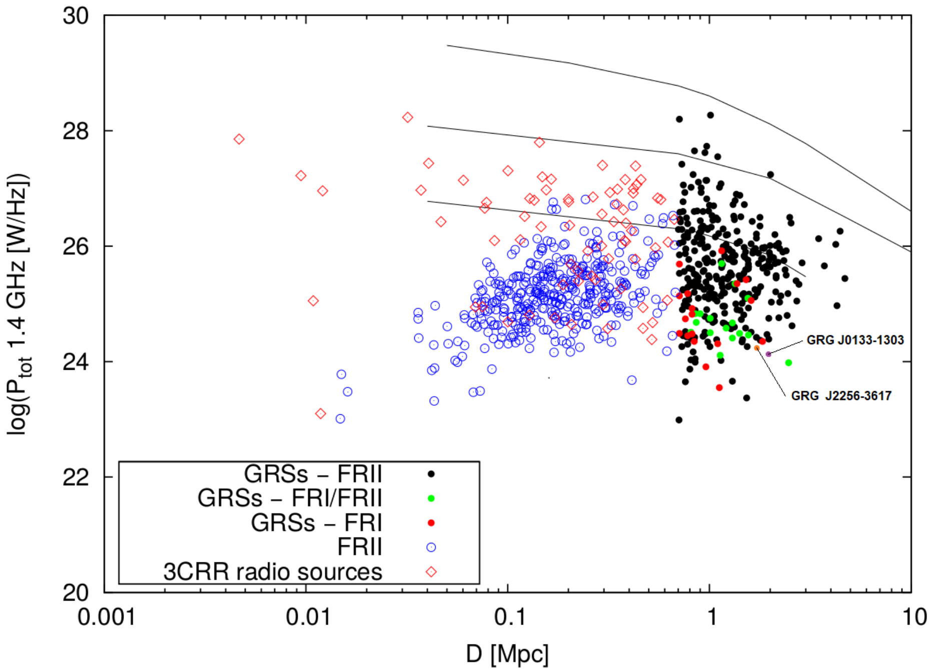

Figure 4.14: P-D diagram with GRG J0133-1303 (purple dot) and GRG J2256-3617 (orange dot) along with other known radio sources and giant radio sources from different papers.

of $\alpha = -0.7 \pm 0.1$, which seems to be in agreement with the average spectral index of the southern lobe. The S4a, S4b, and B sources could be a NAT source with the background source being possible nucleus and S4a and S4b being the lobes. The background source has a steep spectrum and getting much steeper towards S4a and S4b. From the average spectral index of B, S4a, and S4b there is a strong indication that this might be another dying source. The difference in spectral index values obtained from the spectral index map and the plots could be from the way integrated flux densities were measured from the 325 and 610 MHz maps, and associated flux errors. The uncertainties in the estimates of the spectral index might also be due to differences in the uv coverage between the two observations. However, the research study has revealed some information that was missed from GRG J0133-1303 due to poor sensitivity or different frequencies of the KAT-7 instrument.

CHAPTER 5

GRG J2256-3617

The 325 MHz and 610 MHz images of the GRG J2256-3617 were produced using SPAM software. From these images, the core and the lobes of the radio source were detected. Their flux densities together with the uncertainties were determined, and used to compute the integrated spectra. The projected separation between the lobes and the core were determined using CASA software tools, as well as the projected size of the lobes and of the overall GRG. The spectral index map was computed from the uvtaper maps produced using the SPAM pipeline at 325 MHz and 610 MHz map, and the resulting map was used to determine the spectral index of the various components, together with their respective uncertainties.

5.1 RESULTS

5.1.1 Morphology

Figure 5.1 is double extended radio emission 325 MHz image with resolution of 16" × 7" and a rms noise of 0.21 mJy beam^{-1}. From the GMRT 325 MHz contours, the compact region of radio emission can be seen within the southern lobe. This compact region is typical of the hotspot observed in FR II (Fanaroff and Riley, 1974) radio galaxies. The flux density of the various components from this radio source were measured by means of the AIPS tasks IMFIT (point source) and TVSTAT (extended structure). From the 325 MHz image, the northern lobe (including the hotspot) is brighter than the southern lobe with the integrated flux density of 126.9±6.5 mJy, while the southern lobe has a flux density of 115.24±6.03 mJy, and the core is 153.66±0.33 mJy. The projected separation between the lobes and the core was determined using CASA tools, as well as the projected size of the radio lobes and the overall GRG. The angular size and redshift $z \approx 0.09$ were used to determine the projected separation using online cosmology calculator. The northern lobe is 1.4 arcmin away from the core, corresponding to the projected separation of ∼0.15 Mpc, while the southern lobe is 1.5 arcmin away from the core corresponding to projected separation of ∼0.21 Mpc away.

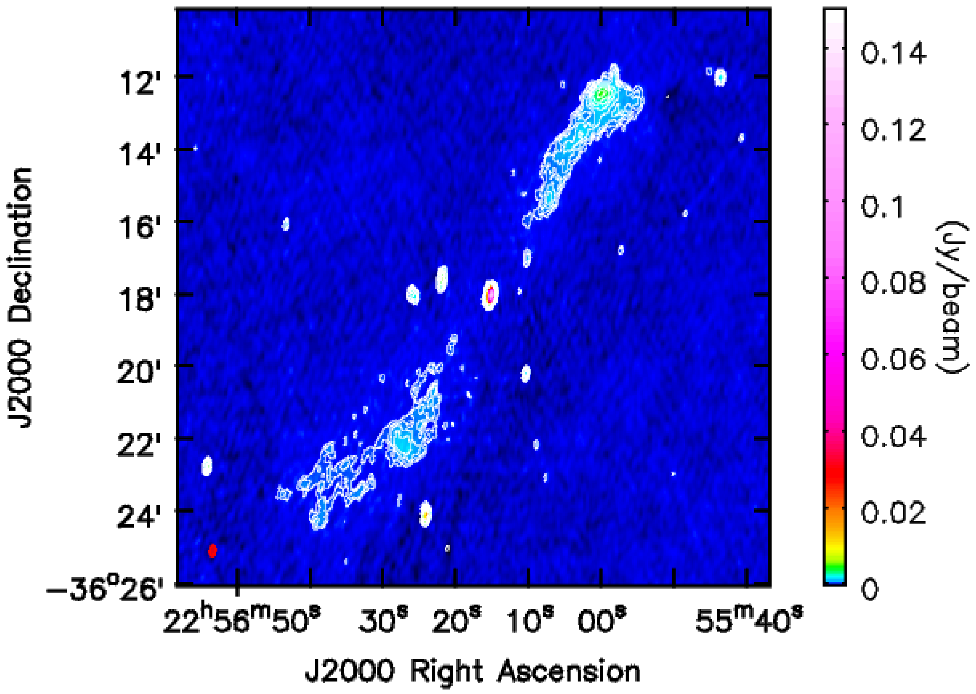

Figure 5.1: The 325 MHz GMRT image with contours overlaid starting from 3σ (σ = 0.13 mJy beam^{-1}) with $\sigma\sqrt{2}$ increments. The beam size 16" x 7" represented in red at the bottom left corner of the image.

Figure 5.2 and 5.3 is 610 MHz image with resolution of 8" × 3" and a rms noise of 0.10 mJy beam^{-1} scaled by factor of $\sqrt{2}$ and 2, respectively. However, in the 610 MHz image the lobes are fainter as compared to the 325 MHz image. The integrated flux density of the core is 149.22±0.61 mJy, which is less brighter as compared to the 325 MHz image, while the northern and southern lobe have the integrated flux density of 52.55±2.69 mJy and 22.53±6.84 mJy, respectively. The northern lobe is brighter, while the southern lobe is not clearly visible in the higher resolution image. The uncertainties of the fluxes were computed using the expression given in equation 4.1, and they are listed in Table 5.1 together with measured flux densities.

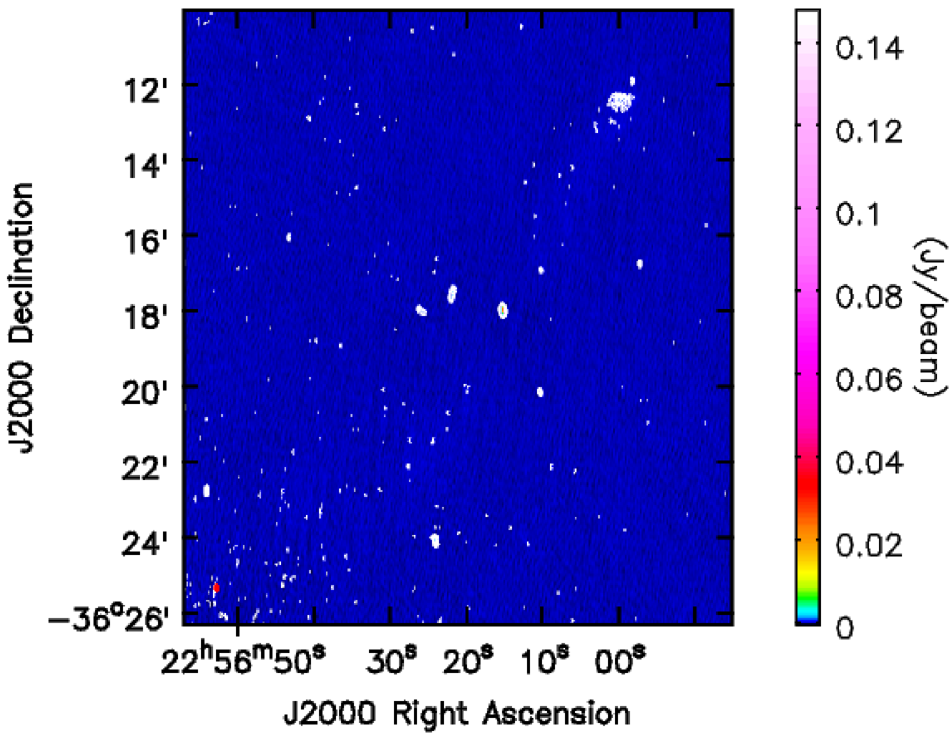

Figure 5.2: The 610 MHz GMRT image with contours overlaid starting from 3σ ($\sigma = 0.10$ mJy beam^{-1}) with $\sigma\sqrt{2}$ increments. The beam size 8" x 3" represented in red at the bottom left corner of the image.

	Core	Northern Lobe	Southern Lobe
Frequency (MHz)	Flux Density (mJy)		
325 SPAM	153.66±0.33	126.9±6.50	115.24±6.03
610 SPAM	149.22±0.61	52.55±2.69	22.53±6.84

Table 5.1: Values of the flux densities of the Core, Northern and Southern lobe.

5.1.2 Multi-frequency Analysis

Figure 5.4 shows the ESO-DSS2-red optical image of GRG J2256-3617 with the UV-Taper GMRT 610 MHz contours overlaid. The optical core has an angular size of ~0.26 arcmin corresponding to the projected size of ~0.03 Mpc and coincide with the core of the radio source as shown in Figure 5.5. The projected separation between the cores is ~0.33 arcseconds. The GRG J2256-3617 has an angular size of ~15.00 arcmin corresponding to the overall projected size of ~1.57 Mpc at redshift $z \approx 0.09$, and is coincident with the reported

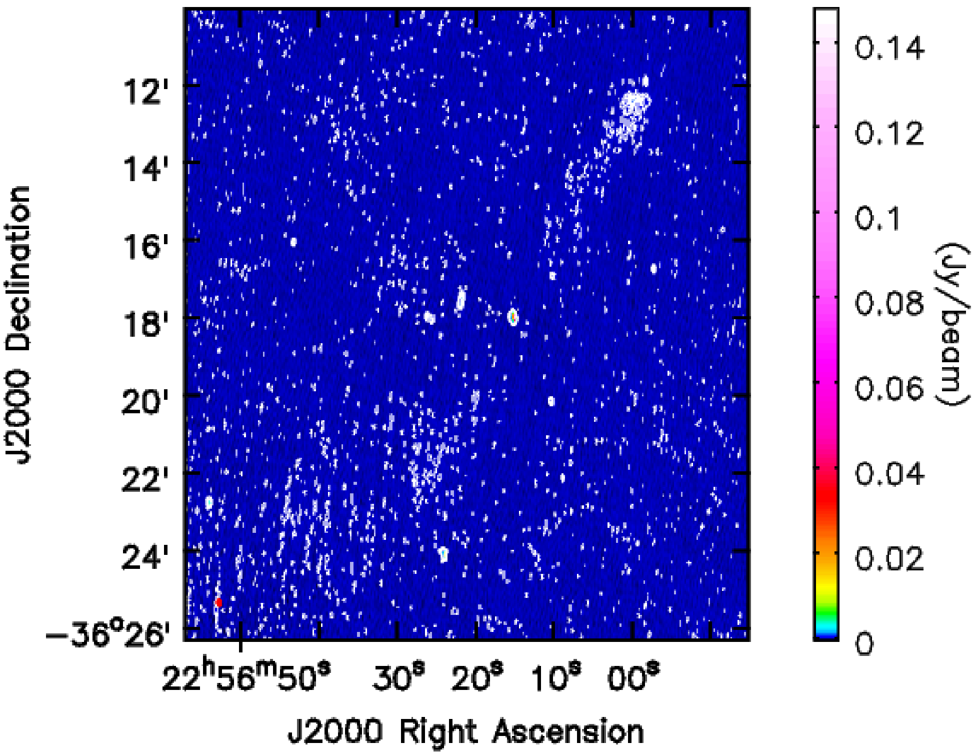

Figure 5.3: The 610 MHz GMRT image with contours overlaid starting at 3σ ($\sigma = 0.10$ mJy beam^{-1}) with 2σ increments. The beam size 8" x 3" is represented in red at the bottom left corner of the image.

value from NVSS catalogue. The northern lobe has an angular size of 4.68 arcmin, corresponding to the projected size of ∼0.49 Mpc, while the southern lobe has an angular size of 2.77 arcmin, corresponding to the projected size of ∼0.29 Mpc.

5.1.3 Integrated Spectra

The flux density scaling was also performed on this radio source. The flux scaling factor was determined by comparing the integrated fluxes of four strong point sources selected from the GMRT at 610 MHz map with counterparts in the GMRT at 325 MHz, TGSS-ADR1 at 150 MHz (Intema *et al.*, 2016), GLEAM surveys from 76 to 227 MHz (Hurley-Walker *et al.*, 2019), and SUMSS at 843 MHz (Mauch *et al.*, 2006), NVSS at 1400 MHz (Condon *et al.*, 1998). The same steps mentioned in section 4.1.3 paragraph 1, were followed to determine the flux scaling factor and perform a position correction on 325 MHz map.

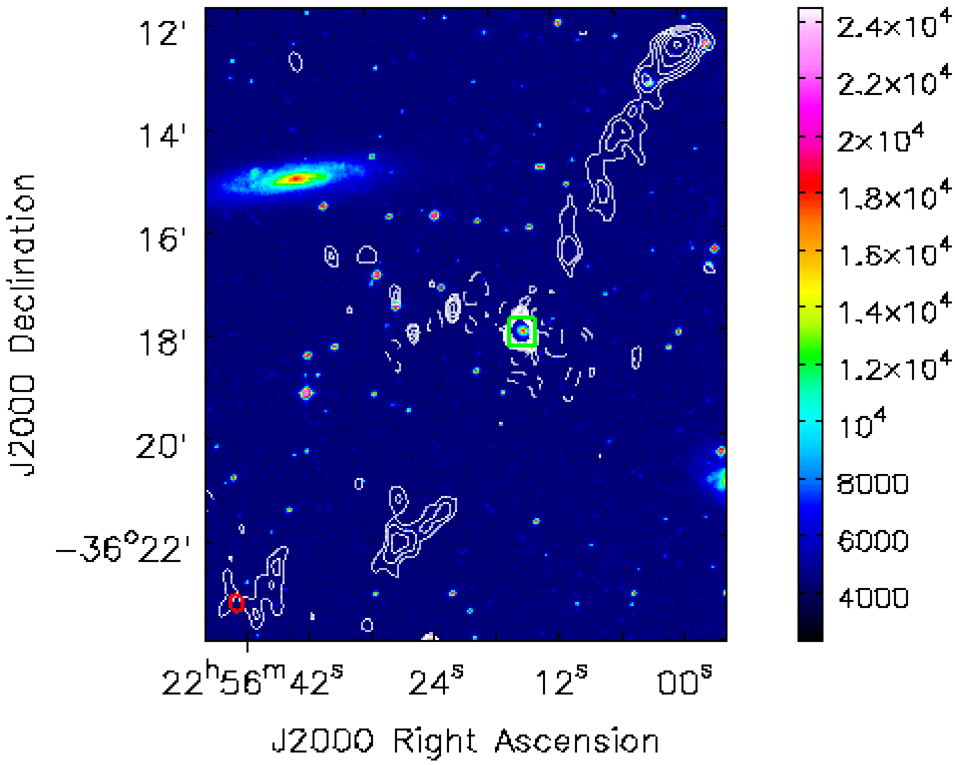

Figure 5.4: Optical source with 610 MHz uv-tapered image contours overlaid starting from 3σ (σ = 0.40 mJy beam^{-1}) with $\sigma\sqrt{2}$ increments. The GMRT 610 beam size 17" x 17" is represented in red at the bottom left corner of the image. The core is indicated in the green box, and the units of the map are given in arcseconds.

Figure 5.6 is a spectrum of the core. The flux density and respective errors from region corresponding to the core were measured from the GMRT map at 325 MHz and 610 MHz, and for TGSS at 150 MHz, SUMSS at 843 MHz, and NVSS at 1400 MHz, the flux densities were obtained from their respective websites. In Table 3.3 we list all flux densities together with their uncertainties from different surveys. The integrated spectra of the northern and southern lobe are shown in Figure 5.7 and 5.8. From the plots the spectral index for northern lobe can be read as $\alpha = -1.63 \pm 0.07$, while for the southern lobe is $\alpha = -1.23 \pm 0.07$.

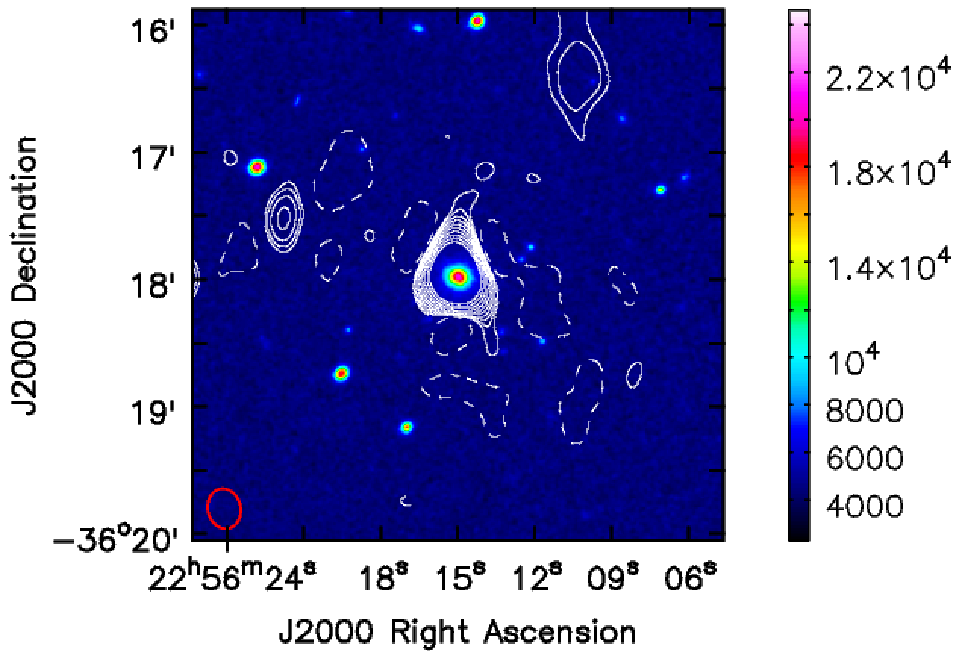

Figure 5.5: A zoom of the optical core with 610 MHz uv-tapered image contours overlaid starting from 3σ (σ = 0.40 mJy beam^{-1}) with $\sigma\sqrt{2}$ increments. The GMRT 610 beam size 17" x 17" is represented in red at the bottom left corner of the image. The units of the map are given in arcseconds.

5.1.4 Spectral Analysis

Figure 5.9 and 5.10 shows UV-taper images at 325 MHz with a rms noise of 0.10 mJy beam^{-1} and 610 MHz with a rms noise of 0.40 mJy beam^{-1} which were used to compute the spectral index image. The images were UV tapered to produce a circular beam of 17" x 17". A two frequency radio spectral index image shown in Figure 5.11 with 610 MHz UV-tapered contours overlaid starting from 3σ (σ = 0.40 mJy beam^{-1}) scaled by $\sigma\sqrt{2}$ was computed using the same steps described in section 4.1.4. The spectral index values were measured using AIPS task TVSTAT for both the lobes and core. The uncertainties of the spectral index value were computed using equation 4.3.

The spectral index of the extended radio source GRG J2256-3617 varies from $\sim \alpha = -0.6$ to $\alpha = 0.2$. The core has an average spectral index of $\alpha = -0.1 \pm 0.01$ which indicate a

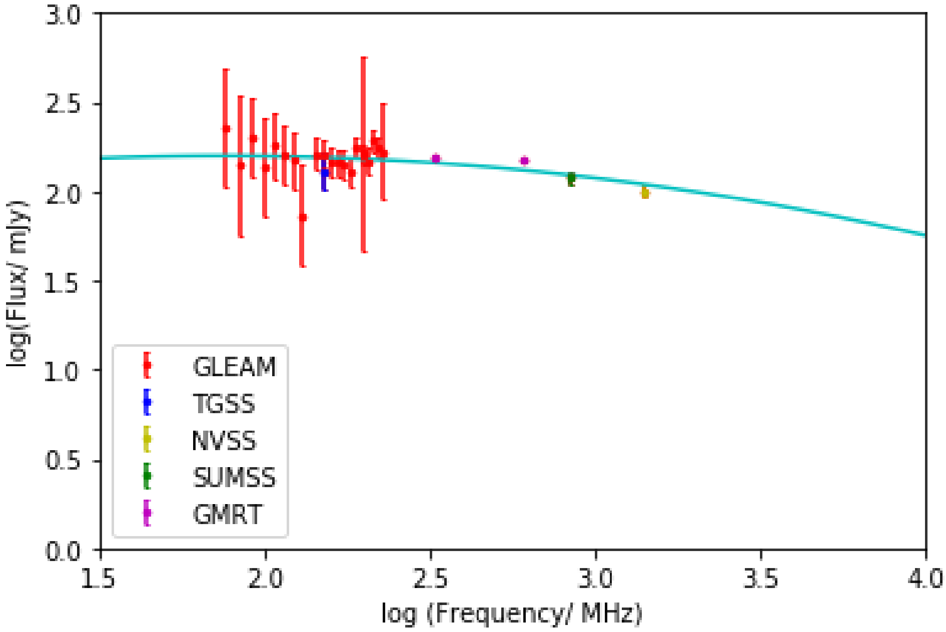

Figure 5.6: Integrated spectra of the core with blue line indicating the best-fit done using log[S/mJy] = -0.10(log[ν/MHz])^2 + 0.37log[ν/MHz] - 1.86.

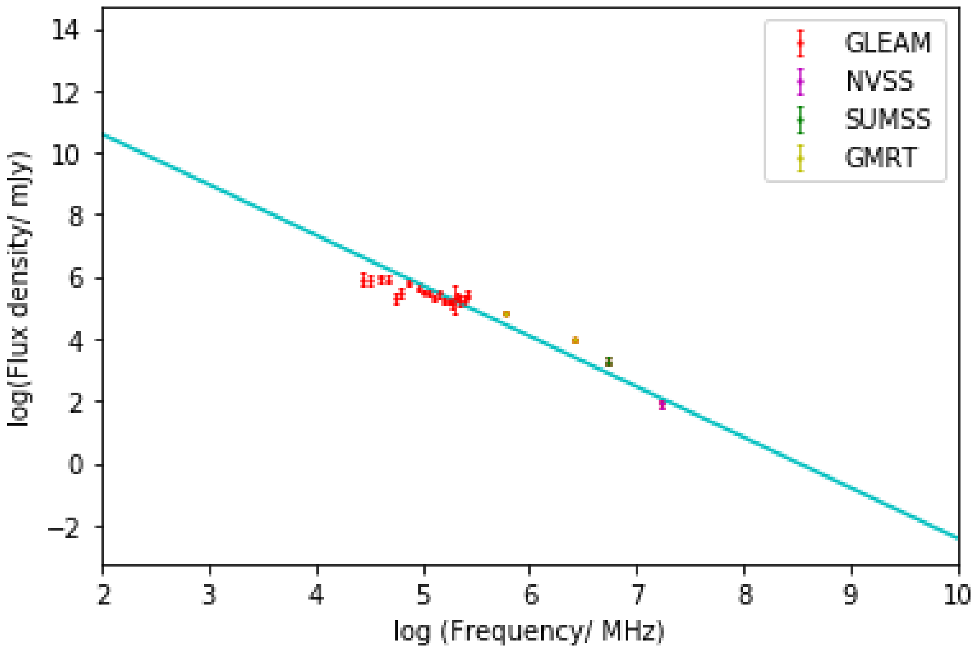

Figure 5.7: Integrated spectra of the northern lobe with blue line indicating the best-fit done using log[S/mJy] = 13.41 - 1.63log[ν/MHz].

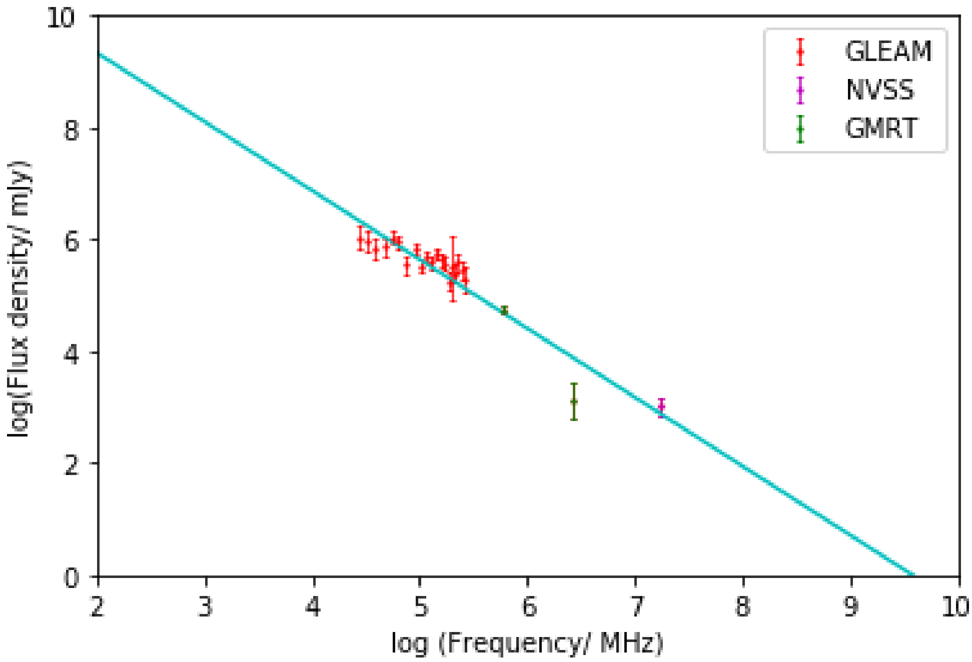

Figure 5.8: Integrated spectra of the southern lobe with blue line indicating the best-fit done using log[S/mJy] = 11.15 - 1.23log[ν/MHz].

flatter spectrum. The northern radio lobe has an average value of $\alpha = -0.2 \pm 0.1$, while the southern lobe which is divided into two components has an average spectral value of $\alpha = -0.01 \pm 0.4$ (including the part close to the core and second part). The part close to the core in the southern lobe has an average spectral index of $\alpha = -0.2 \pm 0.4$, and the second part has an average spectral index of $\alpha = 0.2 \pm 0.4$.

Figure 5.12 its a two frequency radio spectral index images of 325-1400 MHz MHz. The 325 MHz and 610 MHz frequencies are very close, hence, 1400 MHz map was used to compute two frequency radio spectral index of 325-1400 MHz to compare the results. The same steps used to compute the 325-610 MHz spectral index map were followed, in this case the 325 MHz was smoothed to the resolution of 45" x 45" using the imsmooth task in CASA software. From the 325-1400 MHz the core has an average spectral index of -0.3±0.01. The northern lobe has an average spectral index of $\alpha = -0.5 \pm 0.1$, while the southern lobe which is also divided into two components has an average spectral index of $\alpha = -0.6 \pm 0.4$

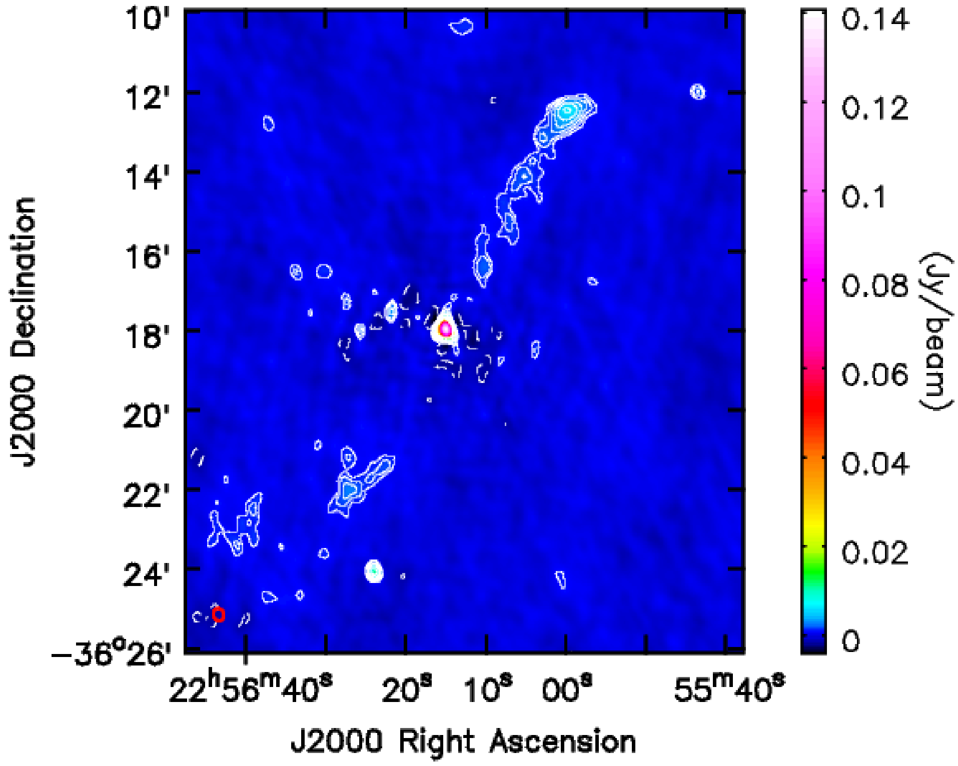

Figure 5.9: The 610 MHz UV-Taper GMRT image overlaid with contours starting from 3σ ($\sigma = 0.40$ mJy beam^{-1}) with $\sigma\sqrt{2}$ increments. The beam size 17" x 17" represented in red at the bottom left corner.

(including the part close to the core and second part). The part close to the core in the southern lobe has an average spectral index of $\alpha = -0.6 \pm 0.4$ and the second part has an average spectral index of $\alpha = -0.5 \pm 0.4$.

5.2 DISCUSSION

In this section the results of GRG J2256-3617 are being discussed by addressing the main objectives and two primary questions mentioned as follows:

1. Search for the radio core, jets, lobes, and characterize the radio source.
2. Determine the type of radio morphology associated with the radio source.
3. Measure the projected size of the GRG.

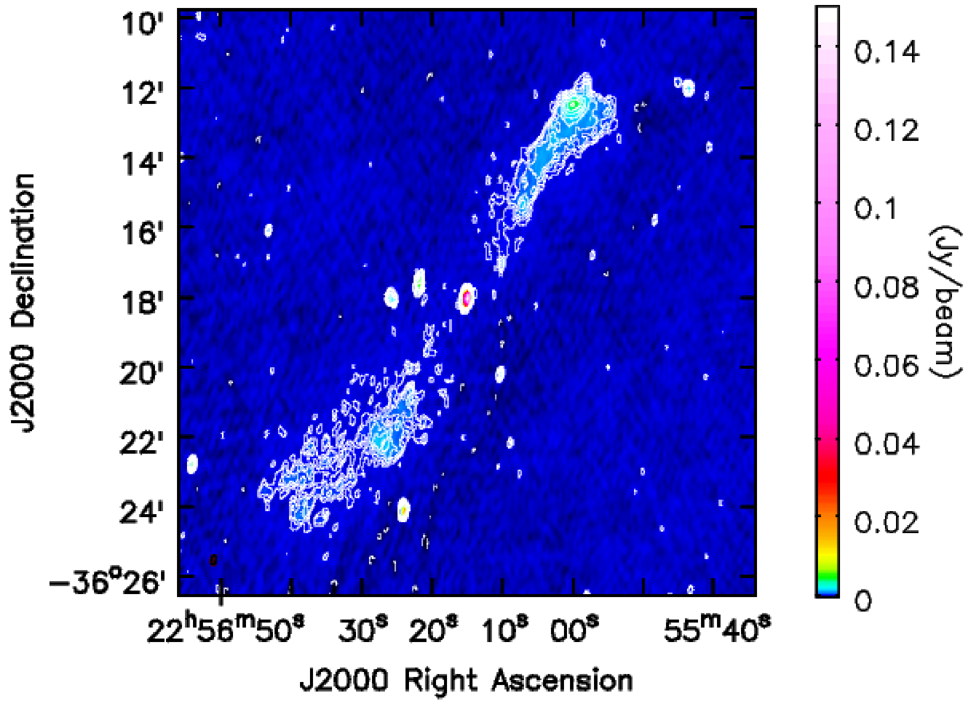

Figure 5.10: The 325 MHz UV-Taper GMRT image overlaid with contours starting from 3σ (σ = 0.10 mJy beam^{-1}) with $\sigma\sqrt{2}$ increments. The beam size 17" x 17" represented in red at the bottom left corner.

4. Perform the spectral analysis of the radio source.

5. What type of radio morphology is associated with the radio source?

6. What is the projected size of the GRG?

This GRG display double-lobed source that are axially symmetric, and edge-brightened indicating the FR II morphology. The hotspot is visible on the southern lobe, however, no jets have been detected, suggesting that there is no pressure being fed to the lobes, and/or the process that create the lobes is no longer active. The contours on the 325 MHz map show evidence of edge brightening in the northern lobe, while the radio lobes are fainter in 610 MHz image. This GRG has a projected size of ∼1.57 Mpc at redshift $z \approx 0.09$, and the radio core coincide with the core of the optical source. The northern lobe has the projected linear size of ∼0.49 Mpc, while the southern lobe is ∼0.29 Mpc. The optical core has projected size of ∼0.03 Mpc and coincide with the core of the radio source.

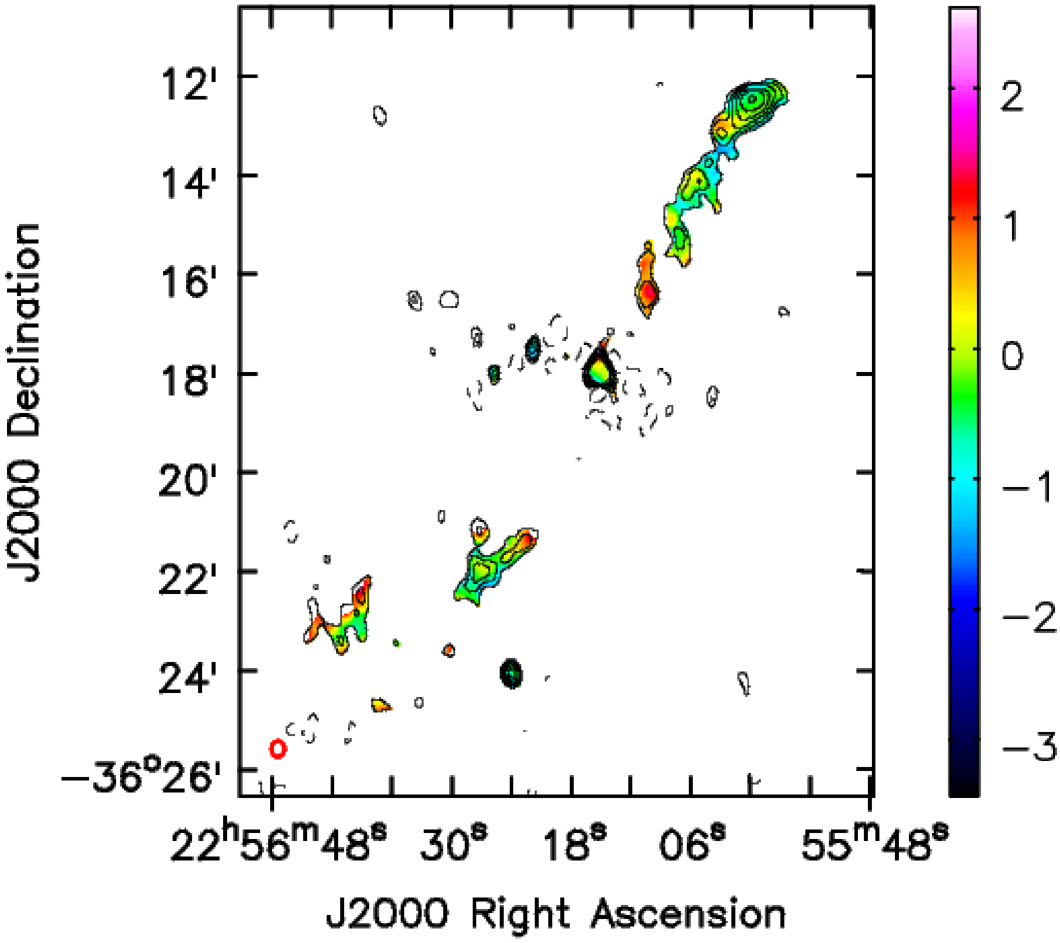

Figure 5.11: 325-610 MHz Spectral index map with 610 MHz contours starting from 3σ (σ = 0.40 mJy beam^{-1}) with $\sigma\sqrt{2}$ increments. The beam size 17" x 17" represented in red at the bottom left corner of the image.

The southern lobe is not clearly visible, this could indicate that the IGM might be relatively less dense to the southern side. The GRG J2256-3617 is indicated by an orange dot in Figure 4.14. Equation 4.4 was used to calculate the radio power of the radio source. At the photometric redshift of $z \approx 0.09$ the radio source has a radio power of $P_{1.4GHz} \approx 0.19$ x 10^{24} W Hz^{-1}, which is compatible with the typical radio powers of the GRGs. The GRG J2256-3617 falls among, and seems to be evolving the same way as other GRGs on the P-D diagram. From the diagram, the radio source has a low radio luminosity at 1.4 GHz fre-

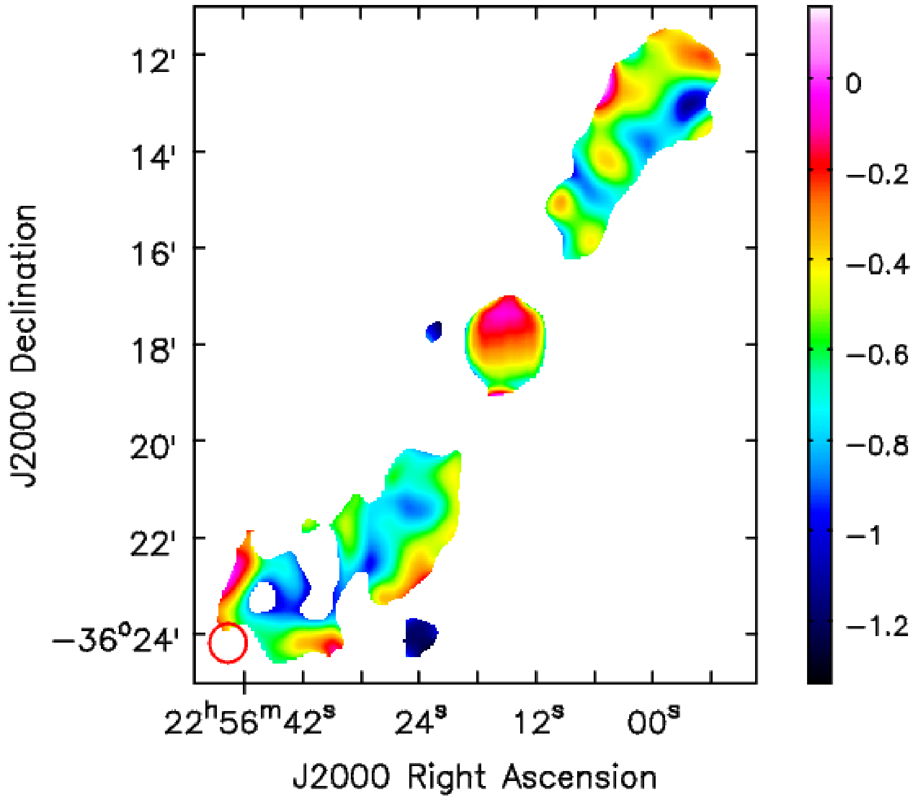

Figure 5.12: 325-1400 MHz spectral index map with a circular beam size 45" x 45" represented in red at the bottom left corner of the image.

quency. This might suggest that as these radio sources evolve to Mpc scales, their radio luminosity decrease. The decrease in radio luminosity might be caused by the radiative energy losses and adiabatic expansion (Dabhade *et al.*, 2017).

The radio core has luminosity of $P_{1.4GHz} \approx 0.32 \text{ x } 10^{25}$ W Hz^{-1}, the northern lobe has the luminosity of $P_{1.4GHz} \approx 5.34 \text{ x } 10^{23}$ W Hz^{-1}, and southern lobe has the luminosity of $P_{1.4GHz} \approx 4.77 \text{ x } 10^{23}$ W Hz^{-1} derived using the source's luminosity distance of 426.95 Mpc. From the spectral index map, the core appears to have flat spectral index. The radio core also appears to have an inverted spectrum, but the integrated flux densities in GLEAM are big with large errors. More data at low frequency is required in order to conclude that the radio core has inverted spectrum. From the 325-610 MHz and 325-1400 MHz spectral index map, the flattest spectral index distribution of the northern lobe suggests the presence of a hotspot at the end of the lobe, while a similar feature is not visible in the southern lobe. The southern lobe on 325-1400 MHz spectral index map indicates the outer region with flat spectral index and get steeper towards the inner regions. The flat spectral index on the outer regions of the lobes results from young plasma, while the steep spectral index towards the inner regions of the lobes is an indication of electrons suffering energy losses and ageing effects. From the Figure 5.7 and 5.8 the radio lobes appears to have steep spectra most possibly due radiative aging caused by old electrons, which causes the frequency break in the spectrum to shift to lower frequencies. This is probably because the electrons were formed earlier and are now suffering energy losses and ageing effects.

Comparing the spectral index of the lobes from the plots with that obtained from the spectral index maps, the values are different. The spectral indices from the spectral index maps are unreliable. The difference in spectral index values could be from the way integrated flux densities were measured from the 325 and 610 MHz maps. The difference in spectral index values from 325-1400 MHz spectral index map could be due to large beam at 1.4 GHz and associated noise. The uncertainties in the estimates of the spectral index might be due to differences in the uv coverage between the two observations. Higher resolution observations at more frequencies are required to study their detailed structure.

CHAPTER 6

CONCLUSION

A follow-up data with GMRT at two different frequencies, i.e 325 MHz and 610 MHz and archive data from NVSS at 1400 MHz, SUMSS at 843 MHz, GLEAM from 76 to 227 MHz, KAT-7 at 1830 MHz and VLASS at 3000 MHz were used to study a previously KAT-7 discovered GRG J0133-1303, and J2256-3617 respectively. This chapter gives a conclusion on the results of GRG J0133-1303 and J2256-3617, described in Chapter 4 and 5.

The research study has revealed some information that was missed from GRG J0133-1303 due to poor sensitivity or different frequencies of the KAT-7 instrument. The northern lobe is divided into four components, S3, S4a, S4b, and the background source (B). No jets and hotspots are detected, suggesting that there is no pressure being fed to the lobes, and/or the process that create the lobes is no longer active. The core has integrated flux density of 7.40 mJy at 325 MHz and 11.97 mJy at 610 MHz (both maps produced using SPAM pipeline). The northern lobe has integrated flux density of 113.18 mJy at 325 MHz and 75.56 mJy at 610 MHz. The northern lobe is brighter than the southern lobe which has integrated flux density of 63.05 mJy at 325 MHz and 46.34 mJy at 610 MHz.

The integrated flux densities of the core, northern and southern lobe from the map produced using AIPS software are 7.8, 108.49, and 65.05 mJy, which is slightly close to integrated flux densities of 325 MHz map produced using a SPAM pipeline, but the northern and southern lobes are brighter as compared to the radio lobes in 610 MHz map. The radio source has overall projected size of $\sim$ 3.59 Mpc at redshift $z \approx 0.3$, while the optical core has projected size of $\sim$ 0.03 Mpc and coincide with the core of the radio source. The northern lobe has a projected size of $\sim$ 1.1 Mpc, while the southern lobe has $\sim$ 0.3 Mpc. The northern lobe is formed far from the radio core, this might suggest that the northern region is relatively less dense medium. The GRG J0133-1303 has radio power of $P_{1.4GHz} \approx 0.16 \text{ x } 10^{24}$ W Hz^{-1}, which is compatible with the typical radio powers of the GRGs.

The GRG J0133-1303 lies among and evolve the same way as other GRGs on the P-D diagram. From the diagram, the radio source has a low radio luminosity at 1.4 GHz frequency. This might suggest that as these radio sources evolve to Mpc scales, their radio luminosity decrease. The decrease in radio luminosity and massive size might be caused by low density environment they expand in. The radio core has luminosity of $P_{1.4GHz} \approx 6.08$ x 10^{24} W Hz^{-1}, while the northern and southern lobe has luminosity of $P_{1.4GHz} \approx 1.12$ x 10^{25} W Hz^{-1}, and $P_{1.4GHz} \approx 0.86$ x 10^{25} W Hz^{-1} derived using the source's luminosity distance of 1598.74 Mpc in the adopted cosmology. The core of the GRG J0133-1303 has an inverted spectrum and flat average spectral index of $\alpha = 0.5 \pm 0.1$ which indicate restarting nuclear activity. The spectral indices of the radio lobes are steep with average spectral index of $\alpha = -0.6 \pm 0.1$ for southern lobe and $\alpha = -0.5 \pm 0.1$ for the northern lobe (S3, S4a and S4b) most possibly due to radiative aging. This is probably because the electrons were formed earlier and are now suffering energy losses and ageing effects.

Not much is known about the GRG J2256-3617, hence the study of this radio source has revealed some detailed information on radio morphology and spectral distribution for the first time. Also no jets are detected in this GRG. The core has integrated flux density of 153.66 mJy at 325 MHz and 149.22 mJy at 610 MHz, which makes the core brighter at 325 MHz. The northern lobe has integrated flux density of 126.9 mJy at 325 MHz and 52.55 mJy at 610 MHz. The northern lobe is brighter than the southern lobe with an integrated flux density of 115.24 mJy at 325 MHz and 22.53 mJy at 610 MHz.

The radio source has overall projected size of $\sim$ 1.57 Mpc at redshift $z \approx 0.09$, while the optical core has projected size of $\sim$ 0.03 Mpc and coincide with the core of the radio core. The northern lobe has a projected size of $\sim$ 0.49 Mpc, while the southern lobe has $\sim$ 0.29 Mpc. The southern lobe appears to fade out indicating the possibility of the IGM being relatively less dense on the southern side. The radio source has a radio power of $P_{1.4GHz} \approx$ 0.19 x 10^{24} W Hz^{-1} at the photometric redshift of $z \approx 0.09$, which is compatible with the typical radio powers of the GRGs. The radio source lies among, and evolve the same way as other GRGs on the P-D diagram. From the diagram, the radio source has a low radio luminosity at 1.4 GHz frequency. This might suggest that as these radio sources evolve to Mpc scales, their radio luminosity decrease. The decrease in radio luminosity and massive size might be caused by low density environment they expand in. The radio core has luminosity of $P_{1.4GHz} \approx 0.32$ x 10^{24} W Hz^{-1}, the northern has the luminosity of $P_{1.4GHz} \approx 5.34$ x 10^{23} W Hz^{-1}, and southern lobe has the luminosity of $P_{1.4GHz} \approx 4.77$ x 10^{23} W Hz^{-1} derived using the source's luminosity distance of 426.95 Mpc.

At this point the radio core appears to have an inverted spectrum, but is not clear because the integrated flux densities from GLEAM are big with large errors. To reach a conclusion, more data at low frequency is required. The radio source has a flat spectral index of $\alpha = -0.1 \pm 0.01$ which indicate restarting nuclear activity. The northern lobe has an average spectral index of $\alpha = -0.2 \pm 0.1$, while the southern lobe has an average spectral of $\alpha = -0.01 \pm 0.4$. Two frequency spectral index map of 325-1400 MHz was also computed. From the 325-1400 MHz the core has an average spectral index of $\alpha = -0.3 \pm 0.01$, while the southern and the northern lobe has an average spectral index of $\alpha = -0.6 \pm 0.4$ and $\alpha = -0.5 \pm 0.1$ respectively. The flat spectral index on the outer regions of the lobes results from young plasma, while the steep spectral index towards the inner regions of the lobes is an indication of electrons suffering energy losses and ageing effects. There is a no much information on this radio source, which makes it a good radio source for future research.

The uncertainties in the estimate of the spectral index on both GRGs which might be due to differences in the uv coverage between the two observations need to be investigated further. However, frequency observations are essential for detailed spectral index maps and to gain further insight into the physical environment of the GRG J0133-1303 and J2256-3617. These radio sources will be perfect objective for the upcoming deep, wide-field surveys such as the MeerKAT deep surveys that will have the potential to study their population evolution up to high redshifts.

REFERENCES

Ananthakrishnan, S. (1995). The giant meterwave radio telescope/GMRT. *Journal of Astrophysics and Astronomy Supplement*, vol. 16, p. 427.

Andernach, H., Jiménez Andrade, E.F., Maldonado Sánchez, R.F. and Vásquez Báez, I.R. (2012). Finding giant radio galaxies in imaging radio surveys. In: *Science from the Next Generation Imaging and Spectroscopic Surveys.*

Bianchi, S., Maiolino, R. and Risaliti, G. (2012). AGN obscuration and the unified model. *Advances in Astronomy*, vol. 2012, id. 782030.

Colafrancesco, S., Mhlahlo, N., Jarrett, T., Oozeer, N. and Marchegiani, P. (2016). Discovery of a suspected giant radio galaxy with the KAT-7 array. *MNRAS*, vol. 456, no. 1, pp. 512–517.

Condon, J.J., Cotton, W., Greisen, E., Yin, Q., Perley, R.A., Taylor, G. and Broderick, J. (1998). The NRAO VLA sky survey. *AJ*, vol. 115, no. 5, p. 1693.

Dabhade, P., Gaikwad, M., Bagchi, J., Pandey-Pommier, M., Sankhyayan, S. and Raychaudhury, S. (2017). Discovery of giant radio galaxies from NVSS: radio and infrared properties. *MNRAS*, vol. 469, no. 3, p. 2886.

Dabhade, P., Mahato, M., Bagchi, J., Saikia, D., Combes, F., Sankhyayan, S., Röttgering, H., Ho, L., Gaikwad, M., Raychaudhury, S. *et al.* (2020*a*). Search and analysis of giant radio galaxies with associated nuclei (SAGAN)–I: New sample & multi-wavelength studies. *A & A*, vol. 642, p. A153.

Dabhade, P., Röttgering, H., Bagchi, J., Shimwell, T., Hardcastle, M., Sankhyayan, S., Morganti, R., Jamrozy, M., Shulevski, A. and Duncan, K. (2020*b*). Giant radio galaxies in the LOFAR Two-metre Sky Survey-I. Radio and environmental properties. *A&A*, vol. 635, p. A5.

De Young, D. (1976). Extended extragalactic radio sources. *Annual Review of Astronomy and Astrophysics*, vol. 14, no. 1, p. 447.

Fanaroff, B.L. and Riley, J.M. (1974). The morphology of extragalactic radio sources of high and low luminosity. *MNRAS*, vol. 167, no. 1, pp. 31P–36P.

Foley, A., Alberts, T., Armstrong, R., Barta, A., Bauermeister, E., Bester, H., Blose, S., Booth, R., Botha, D., Buchner, S. *et al.* (2016). Engineering and science highlights of the KAT-7 radio telescope. *MNRAS*, vol. 460, no. 2, p. 1664.

George, S.J. and Stevens, I.R. (2008). A deep 150 MHz Giant Metrewave Radio Telescope survey in Eridanus. *MNRAS*, vol. 390, no. 2, pp. 741–751.

Hunik, D. and Jamrozy, M. (2016). Discovery of ultra-steep spectrum giant radio galaxy with recurrent radio jet activity in Abell 449. *AJL*, vol. 817, no. 1, p. L1.

Hurley-Walker, N., Hancock, P., Franzen, T., Callingham, J., Offringa, A., Hindson, L., Wu, C., Bell, M., Gaensler, B., Johnston-Hollitt, M. *et al.* (2019). Vizier online data catalog: GLEAM II. galactic plane (hurley-walker+, 2019). *yCat*, pp. VIII–102.

Intema, H. (2014). SPAM: A data reduction recipe for high-resolution, low-frequency radio-interferometric observations. *Astronomical Society of India*.

Intema, H., Jagannathan, P., Mooley, K. and Frail, D. (2016). Vizier online data catalog: The GMRT 150 MHz all-sky radio survey (Intema+, 2017). *VizieR Online Data Catalog*, vol. 359.

Jaffe, W., Meisenheimer, K., Röttgering, H., Leinert, C., Richichi, A., Chesneau, O., Fraix-Burnet, D., Glazenborg-Kluttig, A., Granato, G.-L., Graser, U. *et al.* (2004). The central dusty torus in the active nucleus of NGC 1068. *Nature*, vol. 429, no. 6987, p. 47.

Jaffe, W. and Perola, G. (1973). Dynamical models of tailed radio sources in clusters of galaxies. *A & A*, vol. 26, p. 423.

Jamrozy, M., Saikia, D. and Konar, C. (2009). 4C 02.27: A quasar with episodic activity? *MNRAS*, vol. 399, no. 1, pp. L141–L145.

Jennison, R. and Gupta, M.D. (1953). Fine structure of the extra-terrestrial radio source Cygnus I. *Nature*, vol. 172, no. 4387, pp. 996–997.

Kaiser, C.R., Dennett-Thorpe, J. and Alexander, P. (1997). Evolutionary tracks of FRII sources through the PD diagram. *MNRAS*, vol. 292, no. 3, pp. 723–732.

Kaiser, C.R., Schoenmakers, A.P. and Röttgering, H.J. (2000). Radio galaxies with a 'double-double'morphology—II. The evolution of double-double radio galaxies and implications for the alignment effect in FRII sources. *MNRAS*, vol. 315, no. 2, p. 381.

Kapahi, V. and Ananthakrishnan, S. (1995). Astronomy with the Giant Metrewave Radio Telescope (GMRT). *Bulletin of the Astronomical Society of India*, vol. 23, p. 265.

Komberg, B. and Pashchenko, I. (2009). Giant radio galaxies: Old long-lived quasars? *Astronomy Reports*, vol. 53, no. 12, pp. 1086–1100.

Kozieł-Wierzbowska, D., Asari, N.V., Stasińska, G., Herpich, F.R., Sikora, M., Żywucka, N. and Goyal, A. (2020). Identifying radio active galactic nuclei among radio-emitting galaxies. *arXiv preprint arXiv:2012.00367*.

Krawczynski, H. and Treister, E. (2013). Active galactic nuclei—the physics of individual sources and the cosmic history of formation and evolution. *Frontiers of Physics*, vol. 8, no. 6, pp. 609–629.

Kuźmicz, A., Czerny, B. and Wildy, C. (2019). Stellar populations in hosts of giant radio galaxies and their neighbouring galaxies. *A & A*, vol. 624, p. A91.

Kuźmicz, A., Jamrozy, M., Bronarska, K., Janda-Boczar, K. and Saikia, D. (2018). An updated catalog of giant radio sources. *The Astrophysical Journal Supplement Series*, vol. 238, no. 1, p. 9.

Laing, R., Riley, J. and Longair, M. (1983). Bright radio sources at 178 MHz-flux densities, optical identifications and the cosmological evolution of powerful radio galaxies. *MNRAS*, vol. 204, pp. 151–187.

Laing, R.A. and Bridle, A.H. (1987). Rotation measure variation across M84. *MNRAS*, vol. 228, no. 3, pp. 557–571.

Lara, L., Mack, K.-H., Lacy, M., Klein, U., Cotton, W., Feretti, L., Giovannini, G. and Murgia, M. (2000). The giant radio galaxy 8C0821+ 695 and its environment. *arXiv preprint astro-ph/0002009*.

Leahy, J. (1996). The laing-garrington effect: Implications for tori. *Vistas in Astronomy*, vol. 40, no. 1, pp. 173–177.

Machalski, J., Kozieł-Wierzbowska, D., Jamrozy, M. and Saikia, D. (2008). J1420–0545: The radio galaxy larger than 3C 236. *AJ*, vol. 679, no. 1, p. 149.

Maddox, S.J., Sutherland, W., Efstathiou, G. and Loveday, J. (1990). The APM galaxy survey. I-APM measurements and star-galaxy separation. *MNRAS*, vol. 243, pp. 692–712.

Mahatma, V. (2017). *Spectral ageing in the most powerful radio galaxies.* MA Thesis, University Of Hertfordshire.

Matthews, T.A. and Sandage, A.R. (1963). Optical identification of 3C 48, 3C 196, and 3C 286 with stellar objects. Tech. Rep., Owens Valley Radio Observatory, Pasadena, California.

Mauch, T., Murphy, T., Buttery, H., Curran, J., Hunstead, R., Piestrzynski, B., Ropbertson, J. and Sadler, E. (2006). The Sydney University Molonglo Sky Survey (SUMSS).

Middelberg, Enno & Bach, U. (2008). High resolution radio astronomy using very long baseline interferometry. *Reports on Progress in Physics*, vol. 71, no. 6, p. 066901.

Murphy, E. (2016). The VLA Sky Survey. In: *The many facets of extragalactic radio surveys: towards new scientific challenges*, vol. 267, p. 006. SISSA Medialab.

Nandi, S., Roy, R., Saikia, D., Singh, M., Chandola, H., Baes, M., Joshi, R., Gentile, G. and Patgiri, M. (2014). Discovery of a red quasar with recurrent activity. *The Astrophysical Journal*, vol. 789, no. 1, p. 16.

Nandi, S., Saikia, D., Roy, R., Dabhade, P., Wadadekar, Y., Larsson, J., Baes, M., Chandola, H. and Singh, M. (2019). A low-frequency study of recently identified double-double radio galaxies. *MNRAS*, vol. 486, no. 4, pp. 5158–5170.

Palmer, J. (1996). AIPS–Astronomical Image Processing System. *Starlink User Note*, vol. 207.

Perucho, M., Agudo, I., Alberdi, A., Garcıa-Burillo, S., González-Serrano, J., Márquez, I., Martı, J., Martı-Vidal, I., Mezcua, M., Mimica, P. *et al.* (2015). Active galactic nuclei at kiloparsec scales and their cosmological evolution. *The Spanish Square Kilometre Array White Book*, p. 74.

Peterson, B.M. (1997). *An introduction to active galactic nuclei.* Library of Congress Cataloguing in Publication data. Cambridge University Press. ISBN 0 521 47348 9.

Pradhan, A.K. and Nahar, S.N. (2011). *Atomic astrophysics and spectroscopy.* Library of Congress Cataloguing in Publication data. Cambridge University Press. ISBN 978-0-521-82536-82536-8.

Sadler, E.M. and Hunstead, R. (2002). The Sydney University Molonglo Sky Survey (SUMSS) and optical redshift surveys of the southern sky. In: *Symposium-International Astronomical Union*, vol. 199, p. 11. Cambridge University Press.

Saikia, DJ & Jamrozy, M. (2010). Recurrent activity in active galactic nuclei. *Astronomical Society of India*, vol. 37, p. 63.

Saripalli, L., Subrahmanyan, R. and Shankar, N.U. (2003). Renewed activity in the radio galaxy PKS B1545–321: twin edge-brightened beams within diffuse radio lobes. *AJ*, vol. 590, no. 1, p. 181.

Schoenmakers, A.P., De Bruyn, A., Röttgering, H., Van Der Laan, H. and Kaiser, C. (2000). Radio galaxies with a 'double-double morphology'-I. Analysis of the radio properties and evidence for interrupted activity in active galactic nuclei. *MNRAS*, vol. 315, no. 2, pp. 371–380.

Seyfert, C.K. (1943). Nuclear emission in spiral nebulae. *AJ*, vol. 97, p. 28.

Shields, G.A. (1999). A brief history of active galactic nuclei. *Publications of the Astronomical Society of the Pacific*, vol. 111, no. 760, p. 661.

Wayth, R., Lenc, E., Bell, M., Callingham, J., Dwarakanath, K., Franzen, T., Gaensler, B., Hancock, P., Hindson, L., Hurley-Walker, N. *et al.* (2015). GLEAM: The Galactic and Extragalactic All-sky MWA survey. *Publications of the Astronomical Society of Australia*, vol. 32.

Wright, E.L. (2006). A cosmology calculator for the world wide web. *Publications of the Astronomical Society of the Pacific*, vol. 118, no. 850, p. 1711.